Palaeogeography, Palaeoclimatology, Palaeoecology 702 (2026) 114182

Contents lists available at ScienceDirect

Palaeogeography, Palaeoclimatology, Palaeoecology

journal homepage: www.elsevier.com/locate/palaeo

Paleoenvironmental response in the South China Sea from the Middle Miocene Climatic Optimum to the Middle Miocene Climate Transition: Geochemical records from an isolated carbonate platform

Ning Guo [a], Wei Jiang [a,**], Tianlai Fan [a], Shendong Xu [b], Rui Wang [a], Jian-xin Zhao [c], Yue-xing Feng [c], Kefu Yu [a,b,*]

[a] Guangxi Laboratory on the Study of Coral Reefs in the South China Sea, School of Marine Sciences, Guangxi University, Nanning 530004, China
[b] Southern Marine Sciences and Engineering Guangdong Laboratory (Guangzhou), Guangzhou 528315, China
[c] Radiogenic Isotope Facility, School of Earth and Environmental Sciences, The University of Queensland, Brisbane, QLD 4072, Australia

ARTICLE INFO

Editor: Thomas Steuber

Dataset link: Paleoenvironmental response in the South China Sea from the Middle Miocene Climatic Optimum to the Middle Miocene Climate Transition: Geochemical records from an isolated carbonate platform

Keywords:
Trace elements
Terrigenous input
Paleoproductivity
Redox conditions
East Asian monsoon

ABSTRACT

The middle Miocene climatic optimum (MMCO) to climate transition (MMCT) is a critical Cenozoic turning point, yet its imprint on shallow-water carbonate platforms remains poorly understood. We conducted systematic geochemical analyses (major/trace elements, $\delta^{13}C$, $^{87}Sr/^{86}Sr$) on 13.5–18 Ma carbonates from Well CK2 in the Xisha Islands, South China Sea, to reconstruct the paleoenvironmental evolution of an isolated carbonate platform. Using Al, Ti, Zr to trace terrigenous input, Ni, Cu, $\delta^{13}C$ for marine productivity, and Mn for redox conditions, we identify three evolutionary stages. During 18–17.42 Ma, a weak East Asian summer monsoon (EASM) limited source-area weathering and erosion, maintaining a stable, oligotrophic, and oxic environment with minimal terrigenous input. From 17.42 to 14.87 Ma, intensified EASM precipitation under warm MMCO conditions enhanced chemical weathering and physical erosion, increasing terrigenous detrital flux, as corroborated by elevated $^{87}Sr/^{86}Sr$. The synergy of high sea levels and monsoon-driven upwelling significantly boosted primary productivity. Subsequent organic matter oxygen consumption triggered localized suboxic conditions. Between 14.87 and 13.5 Ma, EASM weakening reduced weathering and erosion, limiting terrigenous material supply. Aeolian sorting during long-distance transport kept Al high while Ti and Zr declined. Concurrently, sea-level fall and weakened upwelling caused a sharp productivity drop. Notably, Mn enrichment persisted, indicating the dominant driver of suboxia shifted from productivity-induced oxygen consumption to restricted water circulation caused by sea-level fall. This study demonstrates that high-resolution geochemical records from isolated platforms effectively capture the coupled responses of terrestrial input, marine productivity, and redox states to middle Miocene monsoon and climate forcing.

1. Introduction

The Middle Miocene Climatic Optimum (MMCO, ~17–14.7 Ma) represents a prominent interval of global warmth within the long-term Cenozoic cooling trend (Shevenell et al., 2004; Steinthorsdottir et al., 2021; Westerhold et al., 2020; Zachos et al., 2001). This period was characterized by elevated atmospheric CO_2 concentrations (van de Wal et al., 2011), depleted deep-sea oxygen isotope values (Zachos et al., 2001), and global mean temperatures approximately 3–6 °C higher than present, accompanied by remarkable changes in global sea-level and deep-ocean circulation patterns (Flower and Kennett, 1994). Multiple regions across the globe responded to the MMCO climate changes: for example, the retreat of the Antarctic ice sheet from the continental shelf to higher elevations in the Transantarctic Mountains (Lewis et al., 2007); enhanced hydrological cycling, weathering, and organic carbon burial in low-latitude regions (Clift et al., 2014; Liu et al., 2024); increased precipitation (Guo et al., 2002; Ma et al., 2022; Zhao et al., 2017); and intensified dissolution of primary minerals in inland Asia

* Corresponding author at: Guangxi Laboratory on the Study of Coral Reefs in the South China Sea, School of Marine Sciences, Guangxi University, Nanning 530004, China.
** Corresponding author.
E-mail addresses: jianwe@gxu.edu.cn (W. Jiang), kefuyu@scsio.ac.cn (K. Yu).

https://doi.org/10.1016/j.palaeo.2026.114182
Received 8 June 2026; Received in revised form 27 August 2026; Accepted 29 August 2026
Available online 1 September 2026

(Li et al., 2023a). Following this greenhouse peak, the Earth's climate crossed a critical threshold and abruptly shifted into the Middle Miocene Climate Transition (MMCT, ~14.7–13.8 Ma). This phase, marked by the rapid expansion of the East Antarctic Ice Sheet and a dramatic drop in global sea level, heralded an irreversible transition of the global climate toward an icehouse state (Shevenell et al., 2008).

As the largest marginal sea in the western Pacific, the environmental evolution of the South China Sea (SCS) is strongly controlled by the East Asian monsoon system, where the seasonal alternation of monsoons profoundly influences regional precipitation patterns, terrigenous sediment transport, and surface ocean circulation (Clift et al., 2014; Wan et al., 2007; Wei et al., 2006). Numerous studies have documented a series of paleoclimatic, geological and paleoceanographic responses of the SCS to the extreme MMCO climate (Clift et al., 2014; Li et al., 2023b; Ma et al., 2023; Shao et al., 2017a, 2017b; Wan et al., 2025; Wan et al., 2009; Wan et al., 2007; Zhang et al., 2025). For instance, based on continuous sedimentary sequences recovered at Ocean Drilling Program (ODP) and International Ocean Discovery Program (IODP) Sites 1146 (Clift et al., 2014), 1148 (Wei et al., 2006), U1499 (Shu et al., 2023) and U1502 (He et al., 2022) in the northern SCS, stepwise changes in chemical weathering indices and clay mineral assemblages suggest that continental weathering, driven by an intensified East Asian monsoon, was significantly enhanced during the MMCO. Furthermore, elevated primary productivity during the MMCO led to increased oxygen consumption in the water column, resulting in anomalous increases in iron fractions and enrichment factors of manganese and uranium (Mn_{EF}, U_{EF}) in SCS deep waters, pointing toward oxygen-depleted conditions (Zhang et al., 2025). Benthic foraminiferal assemblages also record a remarkable decrease in water column oxygenation during this period (Xue et al., 2019). Subsequently, during the MMCT cooling phase, a return to well-oxygenated conditions occurred in response to declining productivity and circulation reorganization (Xue et al., 2019; Zhang et al., 2025).

The vast majority of records documenting the extreme climatic responses of the SCS during the MMCO are derived from deep-sea basin sediments, and direct evidence from in-situ shallow-water environments remains lacking. In fact, shallow-water carbonate platforms have been widely developed across tropical and subtropical oceans since the late Cenozoic (Shao et al., 2017b; Wilson, 2008; Wilson, 2002; Wu et al., 2021), serving as ideal archives for recording the evolution of the global marine environment (Camoin and Webster, 2015; Jiang et al., 2019; Yu, 2012). In recent years, the implementation of multiple scientific drilling programs in the Xisha and Nansha Islands of the SCS (e.g., Wells XK-1 and NK-1) has yielded significant insights concerning isolated carbonate platforms since the early to middle Miocene. These include the establishment of high-precision chronostratigraphic frameworks based on strontium isotope stratigraphy and micropaleontology (Fan et al., 2020; Meng et al., 2022; Su et al., 2024); the response of platform architecture to sea-level fluctuations (Qin et al., 2022; Shao et al., 2017a; Zhao et al., 2026); carbonate factory succession driven by monsoons, temperature, and nutrients (Wu et al., 2021; Wu et al., 2019b; Wu et al., 2019a); as well as seawater chemistry reconstruction, terrigenous input assessment, and diagenetic fluid tracing using geochemical indicators such as isotopes and rare earth elements (Chen et al., 2024; Jia et al., 2024; Jiang et al., 2025; Wu et al., 2024; Xu et al., 2019). However, previous drilling studies of shallow-water carbonate platforms in the SCS have generally lacked high-resolution chronological frameworks, resulting in significant uncertainties in stratigraphic correlation between wells and their precise correspondence with global climatic events. Furthermore, previous research predominantly focuses on sedimentary facies classification, paleontological descriptions, and diagenetic processes, while systematic reconstructions of the paleoenvironment from a geochemical perspective remain relatively limited. Currently, the trace element and isotopic compositions of carbonates have been widely applied in other marine regions to trace paleoceanographic environmental parameters (e.g., Ashok and Absar, 2025; Han et al., 2022; Jiang et al., 2019; Liu et al., 2025; Okafor and Azmy, 2024; Shembilu and Azmy, 2022; Steinmann et al., 2020; Wittkop et al., 2020), yet this approach has not yet been systematically applied to the isolated carbonate platforms of the SCS. In particular, how terrigenous input, productivity, and redox conditions on shallow-water platforms co-evolved during the MMCO to MMCT interval, and the similarities and differences between the paleoenvironmental responses of shallow-water platforms and contemporaneous deep-sea records, have not been explored in depth to date.

To address these gaps, this study focuses on Well CK2, which was drilled in 2013 on an isolated carbonate platform in the Xisha Islands, South China Sea (Fig. 1). The core preserves a continuous carbonate sedimentary record documenting the climatic evolution from the extreme warmth of the MMCO to the icehouse conditions of the MMCT. Here, we conducted systematic major element, trace element and isotopic analyses on carbonate rocks from the 18–13.5 Ma interval of Well CK2. By comprehensively comparing the high-resolution geochemical sequence of Well CK2 with contemporaneous global and regional climatic and oceanographic records, this study reconstructs the stage-wise evolutionary characteristics and driving mechanisms of the paleoenvironment in the Xisha carbonate platform from the MMCO to the MMCT.

2. Regional setting

Located at the junction of the tropical western Pacific and eastern Indian Oceans, the SCS connects to the East China Sea and the Pacific Ocean via the Taiwan and Luzon Straits to the north, and links to the Indian Ocean across the Sunda Shelf to the south. With a total area of approximately 3.5 million square kilometers, it represents one of the largest marginal seas in the western Pacific (Fig. 1A). The East Asian monsoon has existed since the early Miocene or possibly even the Eocene, dominating the climate and marine environment of Southeast Asia (Clift et al., 2014). The seasonal alternation of prevailing winds controls regional precipitation and runoff patterns (Wang et al., 2003; Webster, 1994). Specifically, the East Asian summer monsoon (EASM), associated with continental heating and the development of a low-pressure system over central China, drives mild southwesterly winds across the SCS. Conversely, the East Asian winter monsoon (EAWM) is controlled by continental cooling and the development of the Siberian-Mongolian anticyclonic high-pressure system in northern Asia, generating northeasterly winds across the SCS.

Coral reefs are widely distributed in the SCS, predominantly as fringing reefs, platform reefs and atolls (Yu, 2012), with an evolutionary history that can be traced back to the late Oligocene or early Miocene (Fan et al., 2020). The Xisha Islands (17°07′–15°43′N, 111°11′–112°54′E) are located on a submarine high in the northwestern SCS, representing a group of typical atolls developed on isolated carbonate platforms. Surrounded by deep water basins exceeding 1000 m in depth, this archipelago is situated approximately 300 km from the South China mainland, thereby completely lacking direct terrigenous fluvial input (Fig. 1B). The Xisha Islands experience a tropical monsoon climate, featuring an annual precipitation of 1300–2000 mm, an average annual sea surface temperature of 22–30 °C, and surface salinities ranging from 33.14 to 34.24‰ (Shao et al., 2017b). Such an isolated platform environment, distant from the continent and devoid of coarse terrigenous detrital interference, makes it an ideal archive for recording paleoceanographic evolution and high-resolution climatic signals.

To obtain continuous paleoenvironmental records, drilling of Well CK2 was conducted on Chenhang Island, Xisha Islands, in 2013 (Fig. 1C–D). Drilling commenced at an elevation of +1.0 m above sea level and reached a terminal depth of −928.75 m, penetrating a complete and thick Cenozoic stratigraphic sequence. The average core recovery rate was approximately 70%, with most intervals exceeding 80%. Lithological characteristics indicate that the well profile can be generally divided into two lithologic units: the upper section (0–878.21 m)

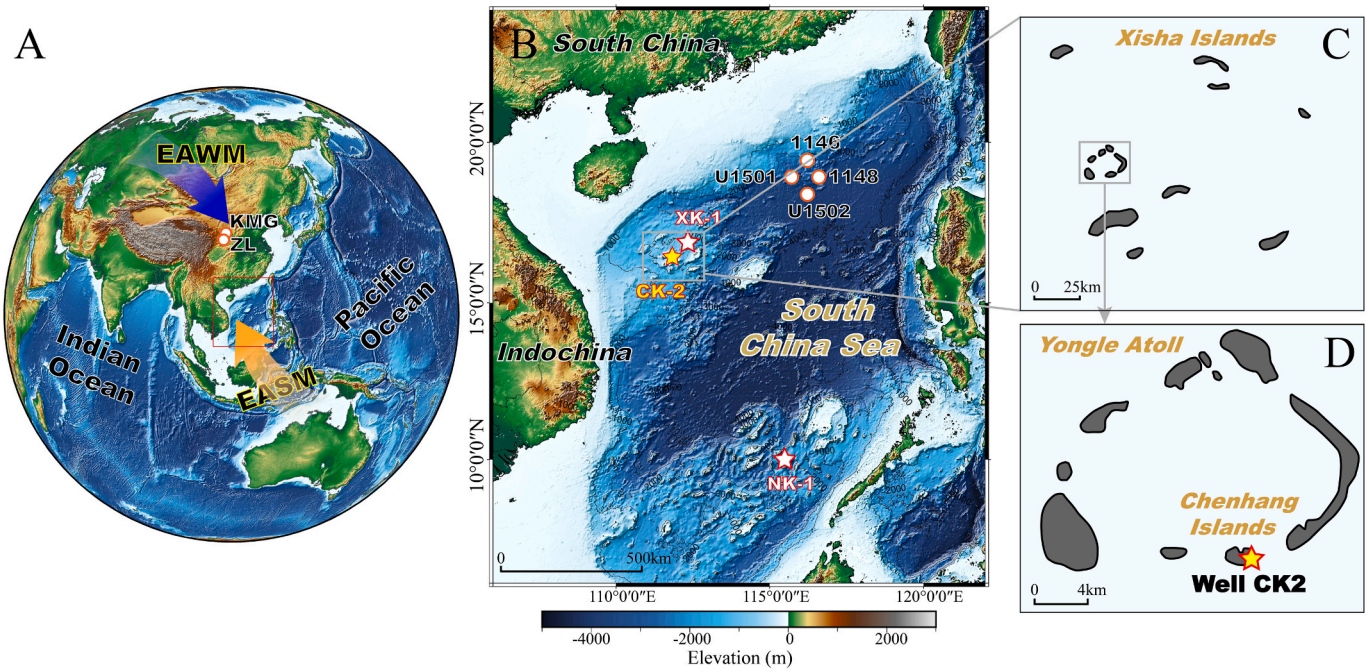

Fig. 1. Overview of the study area. (A) Geographic location of the SCS in a global context. Arrows illustrate the major pathways of the East Asian summer monsoon (EASM) and East Asian winter monsoon (EAWM), respectively. KMG and ZL denote the Kaimengou and Zhuanglang sections on the Chinese Loess Plateau. (B) Topographic map of the SCS, showing the locations of Well CK2 (this study), Well XK-1 and Well NK-1 (stars), and marine drilling sites ODP Sites 1146 and 1148, IODP Sites U1501 and U1502 (circles). (C-D) Enlarged view of the Xisha Islands, showing the specific location of Well CK2 on Chenhang Island, Yongle Atoll.

comprises marine shallow-water carbonate rocks, while the lower section (878.21–928.75 m) consists of basaltic volcaniclastic rocks (Fan et al., 2020). This high-quality, continuous carbonate core provides exceptionally valuable material for reconstructing the regional paleoenvironmental and geological evolution since the early Miocene.

3. Methods

3.1. Major and trace element analyses

A total of 875 representative samples, consisting of corals, coralline algae, and whole-rock matrix sediments, were collected from Well CK2 at a spatial resolution of 1 m. Visibly weathered surfaces were excluded through careful visual checks. Fresh materials were then obtained using a dental drill and ground to powder in an agate mortar. Among these, 213 samples from the 541–803 m interval were selected for paleoenvironmental analysis in this study. All geochemical sample pretreatments and instrumental analyses were conducted at the Guangxi Key Laboratory of Coral Reef Study in the South China Sea, Guangxi University. The related data can be found in Table S1. Detailed procedures are described by Jiang et al. (2019). Note, the major and trace element data from the 541–803 m interval have not been published previously.

To eliminate the interference of residual modern seawater salts and impurities within the pores on geochemical analyses, all carbonate samples were subjected to a desalination pretreatment. An appropriate amount of crushed sample was placed in a beaker, thoroughly mixed with deionized water, and left to stand for 6–8 h before decanting the supernatant. This washing process was repeated three times. Subsequently, the samples were dried in an oven at 100 °C for 24 h and stored in sealed bags for further analysis. Elemental concentrations were determined using an inductively coupled plasma mass spectrometer (ICP-MS). The pretreatment procedures were as follows: 40 mg of the desalinated sample powder, ground to 200 mesh, was accurately weighed and placed into a polytetrafluoroethylene (PTFE) digestion vessel. Next, 2 mL of a mixed acid solution (HF and HNO_3 at a volume ratio of 1:10) was added. The vessel was then sealed and heated on a hot plate at 180 °C for 24 h. The vessel was subsequently opened and evaporated to dryness on the hot plate. Then, 1 mL of H_2O and 1 mL of HNO_3 were added to redissolve the residue on the hot plate at 180 °C for 12 h. Finally, the solution was diluted to a final mass of 80 g with a 2% HNO_3 solution and stored in a refrigerator at 4 °C prior to analysis. To monitor analytical precision and accuracy, one duplicate sample was included for every 20 samples. During the instrumental run, standard and blank samples were analyzed every 20 samples. The final sample results were calibrated against the standards, while precision was controlled using the blanks and duplicates. The relative deviations for all measured elements were less than 10%, fully satisfying the precision requirements. An internal standard solution of Rh (20 ng/L) was added during the analysis to monitor instrumental stability. The national carbonate standard reference materials GBW07129, GBW07133, and GBW07135 were utilized for quality control, yielding relative standard deviations (RSD) of less than 10%, with an average RSD of less than 5%.

3.2. Carbon, oxygen, and strontium isotopic analyses

The $\delta^{18}O$ and $\delta^{13}C$ analyses were carried out at the Guangxi Laboratory on the Study of Coral Reefs in the South China Sea, Guangxi University. Measurements were performed on a Finnigan MAT-253 stable isotope mass spectrometer. The powder samples were reacted with 100% H_3PO_4 at 75 °C to extract CO_2. Isotope ratios are reported relative to the Vienna Pee Dee Belemnite (VPDB) standard. Repeated measurements of the standard reference material GBW04405 ($\delta^{13}C$ = 0.57‰, $\delta^{18}O$ = −8.49‰) yielded standard deviations of 0.03‰ for $\delta^{13}C$ and 0.08‰ for $\delta^{18}O$. Detailed procedures are described by Xu et al. (2019). These $\delta^{13}C$ and $\delta^{18}O$ data from the 541–803 m interval have not been reported previously.

The $^{87}Sr/^{86}Sr$ analyses were conducted at the Radiogenic Isotope Facility of the University of Queensland, Australia. After leaching with dilute acetic acid to remove surface weathering crusts and diagenetic alteration products, the samples were dissolved in acetic acid. The supernatant was separated by centrifugation, evaporated to dryness, and

then redissolved in 2 N HNO_3. Strontium was subsequently separated and purified using Sr-Spec resin columns. The Sr isotopic compositions were determined using a Nu Plasma HR multi-collector inductively coupled plasma mass spectrometer (MC-ICP-MS). The SRM-987 standard was measured before and after every five samples to monitor instrumental drift. The data were corrected for mass fractionation using an exponential law (normalized to $^{86}Sr/^{88}Sr = 0.1194$) and further adjusted for long-term drift using the NIST-987 standard ($^{87}Sr/^{86}Sr = 0.710249$). Approximately 10% of the samples were analyzed in duplicate for quality control. This study utilizes 19 dated samples previously published by Fan et al. (2020) to establish the chronological framework. The remaining anomalous data points deviating from the global seawater $^{87}Sr/^{86}Sr$ evolution curve serve as auxiliary information for paleoenvironmental discussions. An additional 60 $^{87}Sr/^{86}Sr$ data points were previously published by Yang et al. (2022) to further analyze the relationship between $^{87}Sr/^{86}Sr$ anomalies and paleoclimatic and paleoenvironmental conditions. Detailed sample screening criteria, diagenetic evaluations, and dating methodologies are provided by Fan et al. (2020) and Yang et al. (2022).

4. Results

4.1. Petrography and mineralogy

The studied section (541–803 m) is dominated by shallow-marine reef and shoal carbonate limestones, containing abundant biological frameworks and bioclasts, including corals, coralline algae, benthic foraminifera, and bivalves. Specifically, the 541–611 m interval consists mainly of bioclastic rudstone and grainstone. The reef-building organisms in this part are dominated by massive or branching corals and bivalves, showing a relatively shallow and high-energy inner reef flat environment. In contrast, the 611–803 m interval is characterized by frequent interbedding of fine to coarse bioclastic grainstone and rudstone. The grainstone parts are highly enriched in large benthic foraminifera. The rudstone parts (such as branching coral fragments and recrystallized blocks) are commonly wrapped or bound by coralline algae, locally forming dense coralline algal bindstone, which indicates a relatively deeper lagoon environment.

The bulk mineralogical compositions were determined by powder X-ray diffraction (XRD) analysis at the State Key Laboratory of Geological Processes and Mineral Resources, China University of Geosciences, Wuhan. The XRD mineralogical data used in this study have been published previously (Fan et al., 2020). These results show that the carbonate rocks throughout the studied interval (541–803 m) consist almost entirely of stable Low-Magnesium Calcite (LMC), and no significant dolomite was detected. This suggests that unstable components such as aragonite and high-magnesium calcite, originally secreted by organisms, have undergone complete mineral transformation during later diagenesis. Unlike the heavily dolomitized layers above (< 522 m), this interval was not affected by magnesium-rich fluids and preserved a very pure limestone mineral phase.

4.2. Chronological framework

Fan et al. (2020) provided a detailed explanation of the methodology for establishing the chronological framework (Fig. 2). The chronostratigraphic framework of Well CK2 is established primarily through the integration of high-resolution s$^{87}Sr/^{86}Sr$ stratigraphy and magnetostratigraphy. Considering that isolated carbonate platforms are highly susceptible to diagenetic alteration by fluids, a stringent geochemical

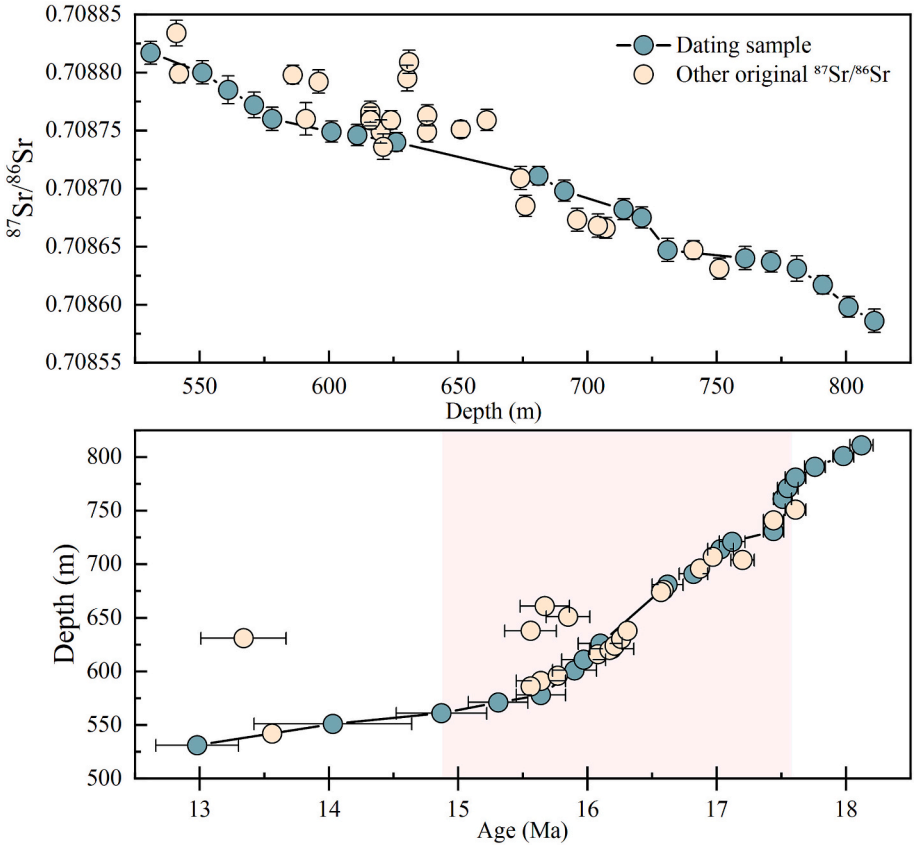

Fig. 2. $^{87}Sr/^{86}Sr$ stratigraphy and chronologic framework of Well CK2. Upper panel: $^{87}Sr/^{86}Sr$ ratios plotted against depth. Lower panel: depth-age relationship established from $^{87}Sr/^{86}Sr$ dating. Green circles represent samples used for dating; yellow circles denote other original $^{87}Sr/^{86}Sr$ data excluded from the age framework. The pink shaded area indicates S2. (For interpretation of the references to colour in this figure legend, the reader is referred to the web version of this article.)

screening was applied to the whole-rock carbonate samples. By evaluating mineralogical characteristics, absolute Sr concentrations (> 300 ppm), and Mn/Sr ratios (below the safety threshold of 2–3), samples significantly contaminated by late-stage diagenetic fluids were identified and excluded. This process ensures that the strontium isotope ratios accurately represent the original seawater composition during the period of deposition. The reliable $^{87}Sr/^{86}Sr$ data were then projected onto the global standard seawater Sr isotope evolution curve (LOWESS) to obtain high-precision age control points. Under these absolute age constraints, combined with stepwise alternating field demagnetization analysis of paleomagnetic inclinations, 10 normal and 8 reversed polarity zones were identified in Well CK2 and accurately correlated with the Geomagnetic Polarity Time Scale (GPTS). This age model indicates that the polarity zones of Well CK2 extend continuously from Chron C6 (approximately 19.60 Ma) at the base to the present. Based on this integrated chronological model, the internal Miocene stratigraphic boundaries in Well CK2 were precisely defined: the Early/Middle Miocene boundary is located at 611 m, and the Middle/Late Miocene boundary is at 522 m.

4.3. Elemental and isotope geochemistry

Based on the abrupt shifts in major and trace elements of carbonates from Well CK2, the elemental concentrations exhibit significant stepwise variations during the 13.5–18 Ma period. Accordingly, the Miocene sequence is divided into three evolutionary stages in this study (Fig. 3): Stage 1 (S1: 18–17.42 Ma), Stage 2 (S2: 17.42–14.87 Ma), and Stage 3 (S3: 14.87–13.5 Ma).

The absolute concentrations of terrigenous detrital indicators (Al, Ti, and Zr) show distinct evolutionary patterns across the three stages (Fig. 3). During S1, the concentrations of Al (mean 127.1 ppm), Ti (mean 4.0 ppm), and Zr (mean 0.31 ppm) generally remain at baseline levels with minor fluctuations. Entering S2 (the MMCO phase), the concentrations of these three elements increase synchronously and sharply. The Al concentration rises rapidly to an average of 445.2 ppm, while Ti and Zr reach high peak values of 28.8 ppm and 1.60 ppm, respectively. However, during S3 (the MMCT phase), a significant decoupling pattern occurs in the elemental evolution. The Al concentration climbs further and stays at a maximum level (mean 721.4 ppm), whereas Ti (mean 19.7 ppm) and Zr (mean 1.0 ppm) do not increase synchronously, showing a clear decline compared to S2.

Trace elements indicating the marine environment (Ni, Cu, and Mn) also display pronounced stage-wise characteristics throughout the three evolutionary stages (Fig. 3). In S1, Ni and Cu concentrations are relatively low and stable (mean Ni 6.8 ppm; mean Cu 0.8 ppm), and the Mn concentration remains at a background level of 12.9 ppm. Moving into S2, Ni and Cu, acting as proxies for paleoproductivity, show synchronous and intense enrichment, jumping to 10.4 ppm and 2.2 ppm, respectively. The Mn concentration exhibits clear fluctuations during this stage (rising to 19.9 ppm), indicating drastic changes in the chemical of the bottom water. In S3, the concentrations of Ni (mean 4.9 ppm) and Cu (mean 0.8 ppm) declined substantially, gradually returning to the baseline levels of S1. Meanwhile, the Mn concentration remains comparable to that in S2, standing at 20.7 ppm.

The $\delta^{13}C$ values of carbonates from Well CK2 range from −4.01‰ to +3.29‰, and $\delta^{18}O$ values range from −7.95‰ to 0.01‰, with a significant positive correlation between the two ($r = 0.74$, $p < 0.01$). The $\delta^{13}C$ values are overall more positive during S2 and shift notably toward more negative values during S3 (Fig. 3). Most of the $^{87}Sr/^{86}Sr$ data excluded from the age framework display elevated values relative to the global seawater Sr isotope evolution curve. These anomalous values are predominantly concentrated in S2 (Fig. 2), indicating an additional source of Sr.

5. Assessment of carbonate purity

Carbonate rocks have the potential to record the geochemical signatures of contemporaneous seawater, yet the reliability of such records

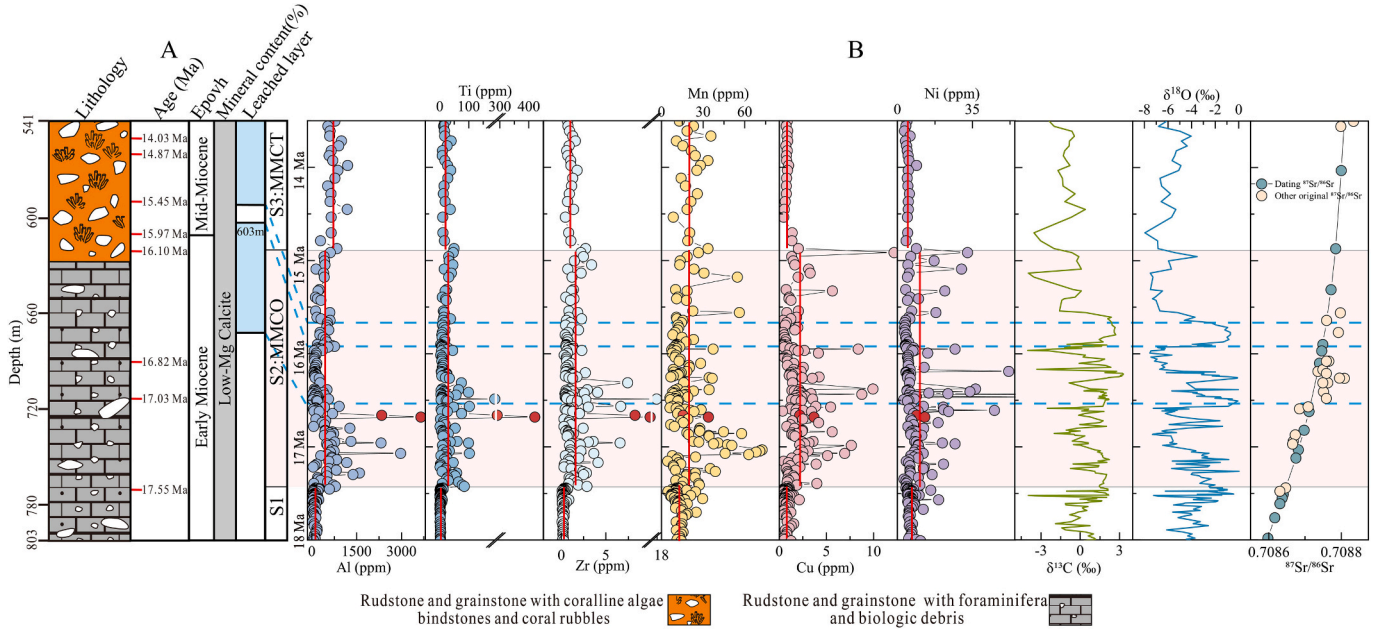

Fig. 3. Multi-proxy geochemical profiles of carbonates (541–803 m) from Well CK2, Xisha Islands. (A) Lithologic column, age (Ma), epoch/stage divisions, mineral compositions (Fan et al., 2020), and locations of exposure surfaces or leached layers. (B) Variations in Al, Ti, Zr, Mn, Cu, Ni, $\delta^{13}C$, $\delta^{18}O$, and $^{87}Sr/^{86}Sr$. For $^{87}Sr/^{86}Sr$ data, green circles represent samples used for dating, and yellow circles denote other original data excluded from the age framework. The sequence is divided into three stages (S1–S3) based on the elemental variations. The pink shaded area (S2) corresponds to the MMCO, and S3 corresponds to the MMCT. An exposure surface identified at 603 m is marked (Yang et al., 2025), with the blue dashed line indicating the depth range affected by subsequent leaching. Red solid lines indicate the mean values of each element for the respective stages. Red dots mark two extreme terrigenous input events at 16.68 Ma and 16.66 Ma, where Al, Ti, and Zr are significantly elevated without concurrent anomalies in Mn, Cu, or Ni. (For interpretation of the references to colour in this figure legend, the reader is referred to the web version of this article.)

depends critically on sample purity. Therefore, the assessment of carbonate purity is an essential prerequisite for paleoenvironmental reconstruction. Only after excluding the incorporation of *syn*-depositional terrigenous detritus and post-depositional alteration (e.g., diagenetic fluid–rock interaction, dolomitization) can the trace element signals recorded in carbonates be reliably used to reconstruct paleoceanographic conditions (e.g., Ashok and Absar, 2025; Hood et al., 2018; Jiang et al., 2019; Shao et al., 2017a; Shembilu and Azmy, 2022; Swart, 2015; Viehmann et al., 2023). Therefore, the reliability of the pristine signals in the carbonate samples from Well CK2 is systematically evaluated below in terms of detrital contamination, dolomitization, and diagenetic alteration.

5.1. Detrital contamination

Immobile elements such as Al, Ti, and Zr are present at extremely low concentrations in seawater and pure marine carbonates, typically several orders of magnitude lower than in terrigenous siliciclastic materials, in which they are predominantly hosted and from which they are delivered to the marine environment via fluvial and/or aeolian transport (Ashok and Absar, 2025; Frimmel, 2009; Han et al., 2022; Nothdurft et al., 2004; Taylor and McLennan, 1985; Webb and Kamber, 2000). Elevated concentrations of immobile elements in whole-rock carbonate analyses are generally attributed to two mechanisms. First, partial dissolution of terrigenous silicates during laboratory acid digestion can artificially inflate measured values, obscuring original seawater signatures (Duda et al., 2014; Nothdurft et al., 2004; Taylor and McLennan, 1985). Second, during early diagenesis, detrital elements can be released into pore waters and incorporated into carbonate crystal lattices (Azmy et al., 2011; Hood et al., 2018; Nothdurft et al., 2004; Zhao and Zheng, 2014). Consequently, evaluating this terrigenous contamination is an essential prerequisite for reliable paleoenvironmental interpretations based on authigenic geochemical signals.

Zr is abundant in shales (210 ppm in the Post-Archean Australian Shale, PAAS; Nothdurft et al., 2004), whereas the Zr concentrations in samples from the studied section are overall extremely low (range 0.07–17.45 ppm, mean 1.2 ± 1.7 ppm). Previous studies have adopted a threshold of Zr < 4 ppm to indicate limited detrital contamination (Han et al., 2022). Among all analyzed samples, only eight data points (approximately 3.7%) exceed this threshold, suggesting that merely a minor fraction of the samples might be affected by terrigenous detrital contamination during digestion. Importantly, despite their relatively higher Al, Ti, and Zr concentrations, the PAAS-normalized rare earth element (REE) patterns of these eight samples all exhibit typical seawater characteristics. These features include light REE depletion, heavy REE enrichment, accompanied by pronounced negative Ce anomalies and positive Y anomalies (Fig. 4). Such patterns demonstrate that the original seawater signals are well preserved within the carbonates (Jiang et al., 2025; Jiang et al., 2019). Notably, two samples at 16.66 Ma and 16.68 Ma record significantly elevated inputs of terrigenous detrital elements (Al, Ti, and Zr), and their PAAS-normalized REE patterns deviate from typical seawater characteristics (Fig. 4). These anomalies likely reflect an extreme event of terrigenous detrital input during the peak warmth of the MMCO (discussed further in Section 6.1). However, even under such extreme terrigenous input conditions, the trace metal concentrations (Mn, Ni, and Cu) in these two samples do not increase synchronously with the immobile elements. Instead, they remain stable within the baseline range of the overall stratigraphic evolution (Fig. 3). If the incorporation of terrigenous detritus had significantly interfered with the trace element signals, a concurrent increase in detritus-derived Mn, Ni, and Cu would be expected, which is not observed. This indicates that even in intervals with the most intense terrigenous input, the geochemical budgets of Mn, Ni, and Cu in the carbonate matrix remain dominated by authigenic components, with a negligible contribution from detrital contamination.

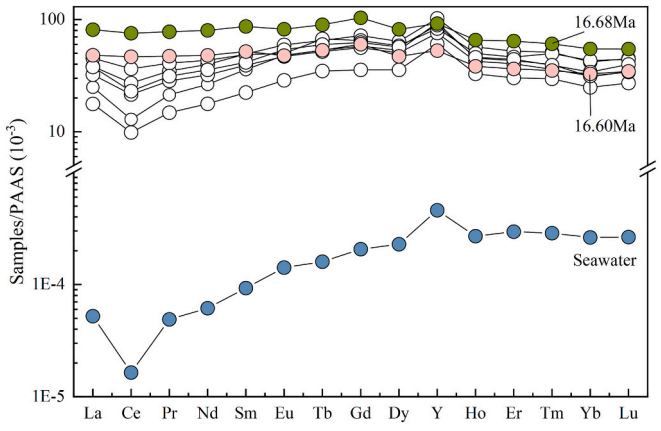

Fig. 4. PAAS-normalized REE patterns of surface seawater samples from the SCS and carbonate samples from Well CK2 with Zr concentrations >4 ppm. Seawater data for the SCS are sourced from Alibo and Nozaki, 2000.

When assessing the interference of terrigenous input on authigenic carbonate signals, a single geochemical threshold (e.g., Zr < 4 ppm) is often of limited utility and should be complemented by multi-proxy cross-validation within the specific geological context. Chenhang Island, where Well CK2 is located, has been separated from the continent since the early Cenozoic and developed on an isolated carbonate atoll in the central SCS. This geographic isolation makes it difficult for terrigenous detritus carried by continental rivers, such as mudstone and sandstone, to reach the site directly (Chen et al., 2024; Jia et al., 2024; Jiang et al., 2019; Shao et al., 2017a). XRD analysis indicates that the mineral composition of the core consists of exceptionally pure calcite (Fig. 3) (Fan et al., 2020), with most samples having CaO ($CaCO_3$) concentrations exceeding 50% (90%) (Fig. 6C), suggesting that the detrital mineral concentration is negligible. Furthermore, analysis of exposure surface samples, which are highly sensitive to weathering and detrital contamination, shows that their major and trace element characteristics do not differ significantly from the rest of the samples (Fig. 3). Together, this evidence confirms the extremely high purity of the carbonate matrix in the studied section.

Correlation analysis further supports this assessment. A highly significant positive correlation exists among Ti, Al, and Zr (Al-Ti: $r = 0.75$; Al-Zr: $r = 0.57$; Ti-Zr: $r = 0.81$), confirming their common terrigenous detrital origin. However, these three elements show only weak or no significant correlation with Mn, Ni, and Cu (Fig. 5). This result indicates that even with fluctuations in terrigenous input, the geochemical budgets of Mn, Ni, and Cu in the carbonates remain dominated by authigenic components and are not interfered with by the admixture of terrigenous detritus. In summary, the trace metals (Mn, Ni, and Cu) in this section are minimally affected by terrigenous silicate detritus and serve as reliable indicators of paleomarine environmental changes. Meanwhile, detrital elements such as Al, Ti, and Zr, which are highly enriched in siliciclastic detritus but present at low levels in the carbonate lattice, are effective proxies for tracking the intensity of terrigenous detrital input (e.g., Han et al., 2022; Jiang et al., 2019; Zhao and Zheng, 2014).

5.2. Dolomitization

XRD mineralogical analysis indicates that the carbonates in the target interval are composed almost entirely of LMC, with no significant dolomite detected (Fan et al., 2020). Given that dolomitization is generally associated with Mg incorporation into precursor carbonates (Brand and Veizer, 1980; Land, 1980), the lack of correlation between CaO and MgO is consistent with the XRD evidence and indicates that dolomitization was negligible in the studied interval (Fig. 6C). In addition, no significant correlation exists between the bulk Mg/Ca ratio and Mn, Ni, or Cu (Fig. 6D–F), indicating that these trace metals were not

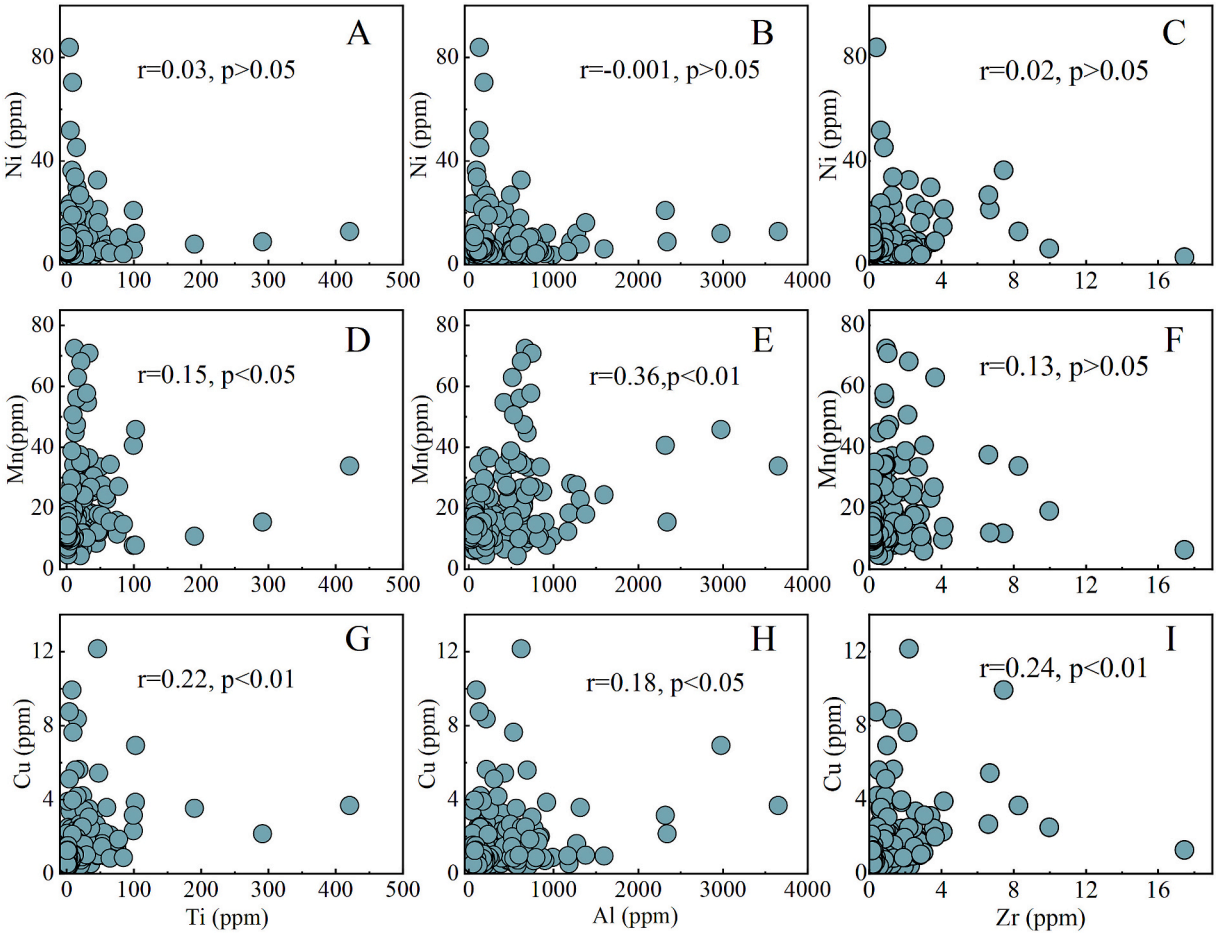

Fig. 5. Cross-plots of geochemical proxies used to evaluate the terrigenous detrital contribution in carbonates from Well CK2. (A–C) Ni vs. Ti, Al, and Zr; (D-F) Mn vs. Ti, Al, and Zr; (G–I) Cu vs. Ti, Al, and Zr. The absence of significant positive correlations among the datasets rules out the interference of terrigenous input on the anomalous enrichment of Ni, Mn, and Cu.

significantly affected by dolomitization.

5.3. Diagenetic alteration

The primary geochemical signals of carbonates are susceptible to diagenetic fluid alteration after deposition. This process can typically be monitored effectively through variations in the concentration of the fluid-mobile element Sr, as well as the $\delta^{18}O$ and $\delta^{13}C$ compositions of the samples (Ashok and Absar, 2025; Brand and Veizer, 1980; Chen et al., 2024; Derry, 2010; Jacobsen and Kaufman, 1999; Zhang et al., 2024). Meteoric fluids are generally characterized by relatively depleted $\delta^{18}O$ and $\delta^{13}C$ values. During fluid-rock interactions, they cause the isotopic composition of diagenetic carbonates to evolve toward more negative values while leaching Sr from the primary crystal lattice (Brand and Veizer, 1980; Derry, 2010; Li et al., 2013; Veizer et al., 1999). On the other hand, diagenetic fluids in deep burial reducing environments are enriched in Mn, which can be introduced into the carbonate lattice to further replace Sr (Banner and Hanson, 1990; Derry, 2010; Gilleaudeau and Kah, 2013). Both processes lead to a decrease in Sr and an increase in Mn concentrations in secondary carbonates, manifesting as a significant negative correlation between Mn and Sr and a sharp increase in the Mn/Sr ratio.

In the studied section, the Sr concentration shows a negative correlation with $\delta^{18}O$ ($r = -0.39$, $p < 0.01$; Fig. 7H), and a strong covariation exists between $\delta^{13}C$ and $\delta^{18}O$ ($r = 0.74$, $p < 0.01$; Fig. 7G). These features indicate that the carbonates from Well CK2 did experience post-depositional fluid-rock interactions, primarily characterized by the alteration of fluid-mobile elements and isotopic compositions by meteoric water. However, if Mn, Ni, and Cu had been significantly mobilized during diagenesis, they would be expected to show strong correlations with the above diagenetic indicators. The actual analytical results reveal a weak positive correlation between Mn and Sr ($r = 0.17$, $p < 0.05$; Fig. 7I), rather than the negative correlation expected from diagenetic replacement. Furthermore, Mn shows no correlation with either $\delta^{18}O$ or $\delta^{13}C$, suggesting that variations in Mn concentration were more likely controlled by the redox conditions of the water column during deposition rather than by later-stage diagenetic fluid alteration. Similarly, neither Ni nor Cu exhibits significant correlations with $\delta^{18}O$ and $\delta^{13}C$ (Fig. 7), nor do they show strong correlations with the Mn/Sr ratio (Fig. 6A-B). This further confirms that these trace metals were not affected by diagenetic fluid-rock interactions.

Additionally, traditional empirical thresholds are employed to further evaluate the extent of diagenetic alteration. Mn/Sr ≈ 1 and $\delta^{18}O$ ≈ −10‰ are generally considered diagnostic criteria for ancient carbonates that have undergone severe burial diagenesis and meteoric alteration (Higgins et al., 2018). The $\delta^{18}O$ values of the studied samples range from −7.95‰ to 0.01‰ (mean −4.05‰), well above the lower limit of −10‰. The Mn/Sr ratios range from 0.005 to 0.183 (mean 0.05), far below the threshold of 1 (Fig. 7I), demonstrating that this section has not experienced severe destructive diagenetic alteration. In summary, although meteoric fluids have to some extent modified the Sr concentrations and $\delta^{18}O$ and $\delta^{13}C$ compositions of the carbonates in Well CK2, the target trace elements of this study (Mn, Ni, Cu) have not been significantly affected. Unlike highly fluid-mobile elements such as Sr,

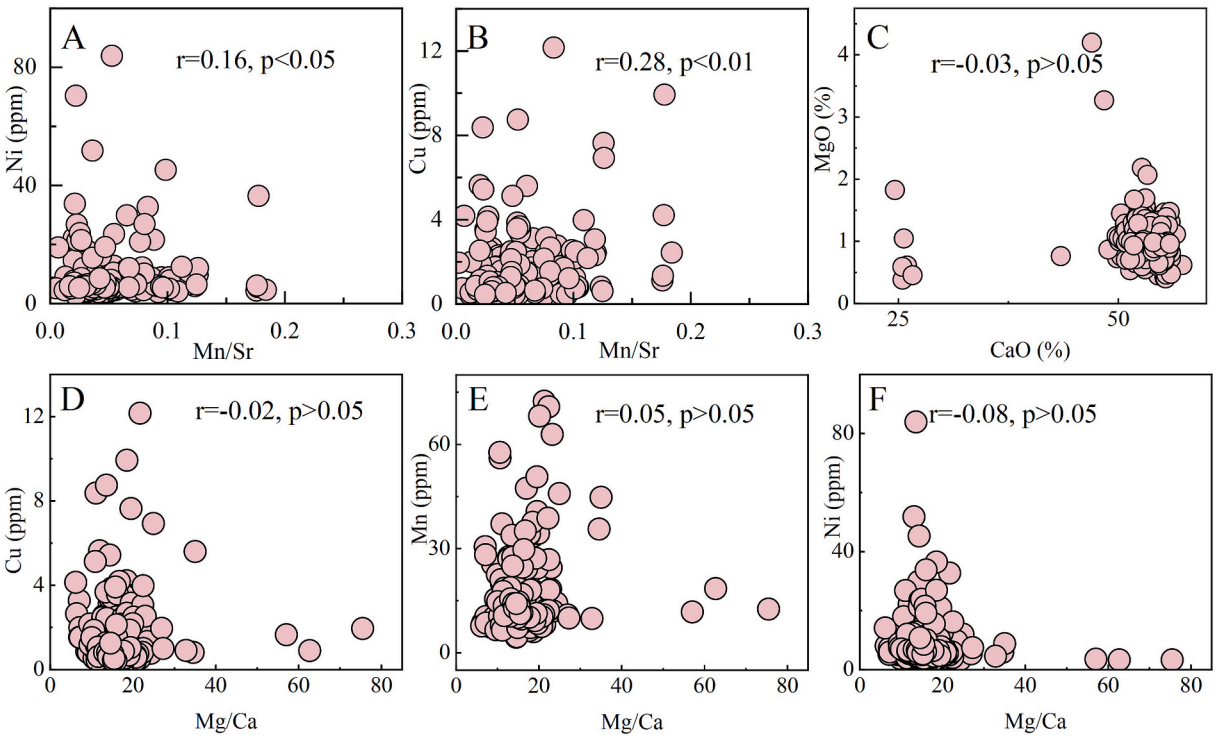

Fig. 6. Geochemical cross-plots assessing dolomitization and its impact on trace elements in carbonates from Well CK2. (A-B) Mn/Sr vs. Ni and Cu; (C) MgO vs. CaO; (D-F) Mg/Ca vs. Ni, Cu, and Mn.

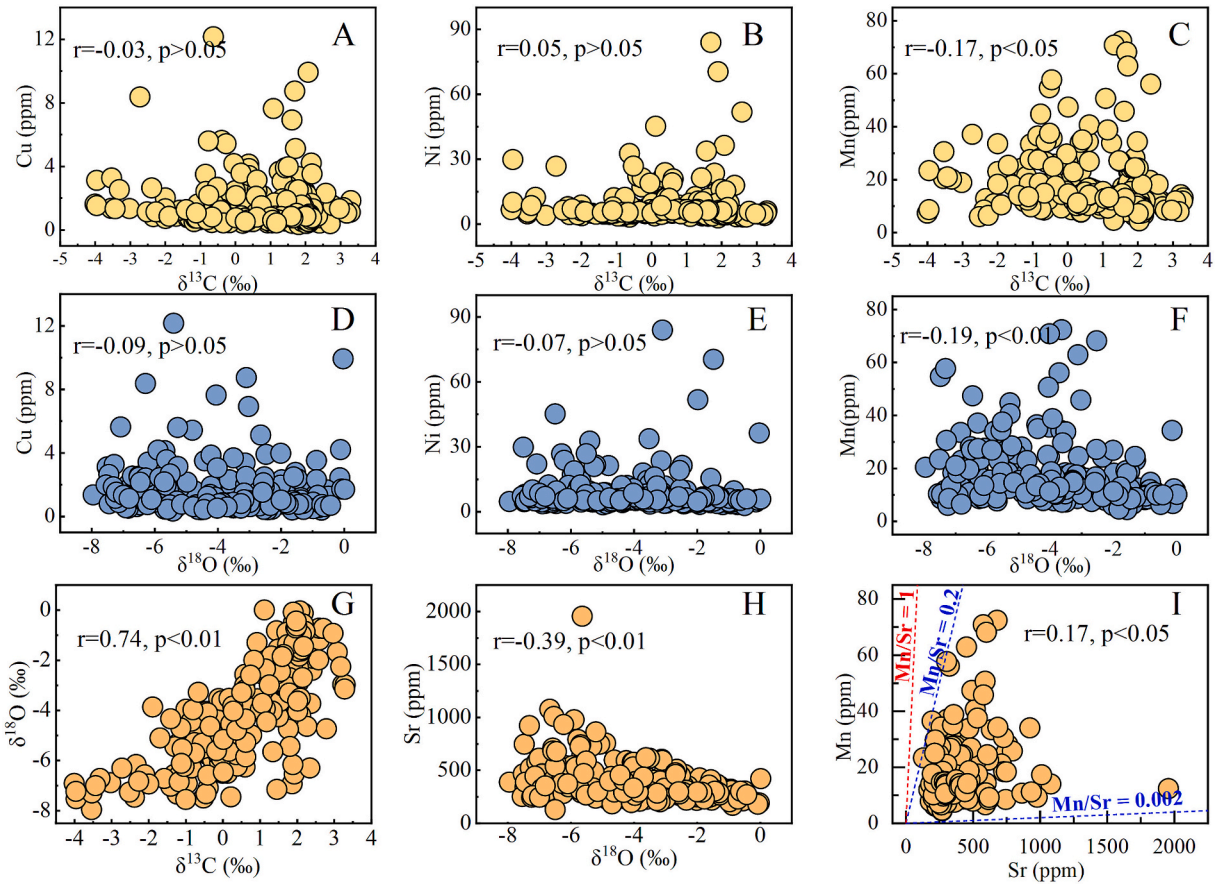

Fig. 7. Geochemical cross-plots for the comprehensive assessment of diagenesis in carbonates from Well CK2. (A-C) $\delta^{13}C$ vs. Cu, Ni, and Mn; (D-F) $\delta^{18}O$ vs. Cu, Ni, and Mn; (G) $\delta^{13}C$ vs. $\delta^{18}O$; (H) Sr vs. $\delta^{18}O$; (I) Sr vs. Mn.

the primary seawater chemical signals of Mn, Ni, and Cu are well preserved, serving as reliable proxies for subsequent high-resolution paleoenvironmental reconstructions.

6. Discussion

Based on the carbonate purity assessment presented above, the geochemical proxies from Well CK2 are divided into two groups for paleoenvironmental interpretation: (1) terrigenous detrital indicator elements (Al, Ti, Zr), used to trace variations in the intensity and transport modes of terrigenous material input; (2) seawater environmental indicator (Mn, Ni, Cu), reflecting changes in water-column redox conditions and marine primary productivity, respectively.

As a redox-sensitive element, Mn exists in the soluble Mn^{2+} form under reducing conditions (Tribovillard et al., 2006) and is more readily incorporated into the carbonate lattice. Therefore, elevated Mn concentrations in carbonates typically indicate enhanced reducing conditions in the water column during deposition. The lack of correlation between Ni or Cu and the detrital elements rules out significant terrigenous contributions to their concentrations. Ni and Cu also display no significant correlation with Mn, indicating that they were not incorporated into the carbonates via adsorption–coprecipitation with Mn oxides. Ni and Cu are predominantly present as organometallic complexes and are transferred from surface waters to sediments through phytoplankton uptake and organic matter adsorption, making them widely recognized as reliable proxies for biological productivity (Arnaboldi and Meyers, 2007; Okafor and Azmy, 2024; Smrzka et al., 2019; Tribovillard et al., 2006). The positive correlation between Ni and Cu ($r = 0.55$, $p < 0.01$) indicates that both are governed by the same biogeochemical process. The strong positive intercorrelations among the terrigenous indicator group confirm their common detrital origin, while the weak or insignificant correlations between the two groups of elements demonstrate that the terrigenous input signal and the seawater environmental signal are essentially independent in the studied section. In addition to the trace element proxies, the $\delta^{13}C$ record is used to provide information on carbon cycling and productivity changes, while anomalous $^{87}Sr/^{86}Sr$ values are employed to assess terrigenous detrital input. The complete major and trace element profiles are presented in Fig. 3. For clarity in the subsequent discussion, selected proxies are compiled in Figs. 8–10 alongside regional and global records.

6.1. Middle Miocene climatic and environmental changes and terrigenous input

The terrigenous input indicated by Al, Ti, and Zr in Well CK2 exhibits a clear three-stage evolutionary pattern (Figs. 3, 8): concentrations are extremely low in stage S1, increase significantly to a peak in early stage S2 before gradually declining, and decrease markedly in stage S3. To further explore the intrinsic link between the Middle Miocene climate evolution and terrigenous detrital input in the northern SCS, a series of global and regional climatic and environmental records are comprehensively compared in this study (Fig. 8).

The Xisha Islands are located on an isolated submarine plateau in the northern SCS, separated entirely from the continent by surrounding waters with depths exceeding 1000 m, lacking direct terrestrial river discharge (Fig. 1B). Under such a geographic configuration, the arrival of fine-grained suspended matter discharged by surrounding rivers into the SCS and transported by ocean currents to the carbonate platform via distal diffusion would be expected to be extremely limited (Chen et al., 2024; Jiang et al., 2019). Previous studies have demonstrated that atmospheric dust driven by the EAWM can be transported over long distances and deposited onto the Xisha Islands (Liu et al., 2014), suggesting that this pathway is likely the most important source of terrigenous detritus on the Xisha platform. End-member modeling analysis of grain size at ODP Site 1146 reveals that aeolian dust from inland Asia and fluvial inputs account for approximately 20% and 80% of the total terrigenous material at that site, respectively (Wan et al., 2007). Given that Well CK2 is located farther from the continent and more distant from river mouths than ODP Site 1146, the contribution from distal diffusion of fluvial suspended matter is likely even more limited, and the relative importance of aeolian dust deposition correspondingly greater. The long-distance transport of dust is a complex process, influenced by source area environmental conditions, transport dynamics, and the regional climate of the depositional area (Liu et al., 2014). The aeolian dust flux reaching Well CK2 is therefore governed by two key factors: the supply of terrigenous detritus from the source region and the efficiency of wind in transporting dust over long distances to the Xisha Islands. The former is primarily controlled by the EASM, whose rainfall intensity determines the rates of continental chemical weathering and physical erosion and hence the volume of terrigenous products (Clift et al., 2014). The latter is mainly controlled by the EAWM, which provides the strong northerly winds that serve as the principal driving force for the long-distance southward transport of continental dust to the SCS (Wan et al., 2007). However, no consensus has yet been reached on whether the EAWM continuously strengthened or weakened during the middle Miocene. Aeolian dust accumulation fluxes on the Chinese Loess Plateau and in the North Pacific increased substantially overall during ~21–13 Ma, suggesting sustained strengthening of the EAWM (Guo et al., 2002; Wan et al., 2025). In contrast, many recent studies suggest that the EAWM strengthened before the MMCO, became stable or relatively weaker during the MMCO, and intensified significantly during the MMCT (e.g., Li et al., 2023b; Lu et al., 2026; Miao et al., 2011). Multiproxy analysis of ODP Site 1146 by Wan et al. (2007) also indicates that the intensity of the EAWM relative to the EASM underwent a profound shift at approximately 15 Ma since 20 Ma. To further test whether EAWM transport efficiency was the dominant control factor for terrigenous input to the Xisha platform, we compared Al and Zr concentrations in Well CK2 with two independently reconstructed records of EAWM intensity (Fig. 9). The EAWM evolutionary pattern revealed by these records was inconsistent with the variation trends of the terrigenous input proxies in Well CK2, where the EAWM was stronger but aeolian dust input was the lowest during stage S1, whereas the EAWM was stable or weaker but aeolian dust input reached its maximum during stage S2. Therefore, this relationship does not support variations in the transport efficiency of the EAWM as the dominant driver of aeolian input to the Xisha area during the middle Miocene. However, during early S2, several intervals of enhanced EAWM intensity show local temporal correspondence with high Al, Ti, and Zr concentrations in Well CK2, indicating that, when source-material supply was sufficient, short-term strengthening of the EAWM may have made a transient contribution to aeolian dust flux (Figs. 3, 9).

We therefore conclude that the enhanced continental weathering and physical erosion driven by the EASM, together with the resulting increase in terrigenous material supply, serve as the primary factor controlling the input of terrigenous material into the Xisha carbonate platform. The global benthic foraminiferal oxygen isotope record (Fig. 8I; Zachos et al., 2001) and mean seawater temperature reconstructions (Fig. 8J; Song et al., 2019) indicate that global warming reached its peak during ~17–14.7 Ma (Wu et al., 2025). Throughout Earth's history, warm and humid climates have generally been associated with an intensified hydrological cycle and enhanced chemical weathering (White and Blum, 1995), a relationship that has been widely confirmed across multiple global warming events (Algeo and Twitchett, 2010; Bottini et al., 2012; Clift et al., 2014; Han et al., 2022; Pogge von Strandmann et al., 2013; Wu et al., 2025). However, the anomalously strong EASM and extreme weathering during the middle Miocene were not simply a passive response to global warming. The Cenozoic uplift of the Himalayas and Tibetan Plateau has long been widely regarded as a critical driver for the intensification of the East Asian monsoon (An et al., 2001; Prell and Kutzbach, 1992). Paleoaltimetric reconstructions based on plant fossils suggest that the main bodies of the Himalayas and the Tibetan Plateau had already reached elevations of

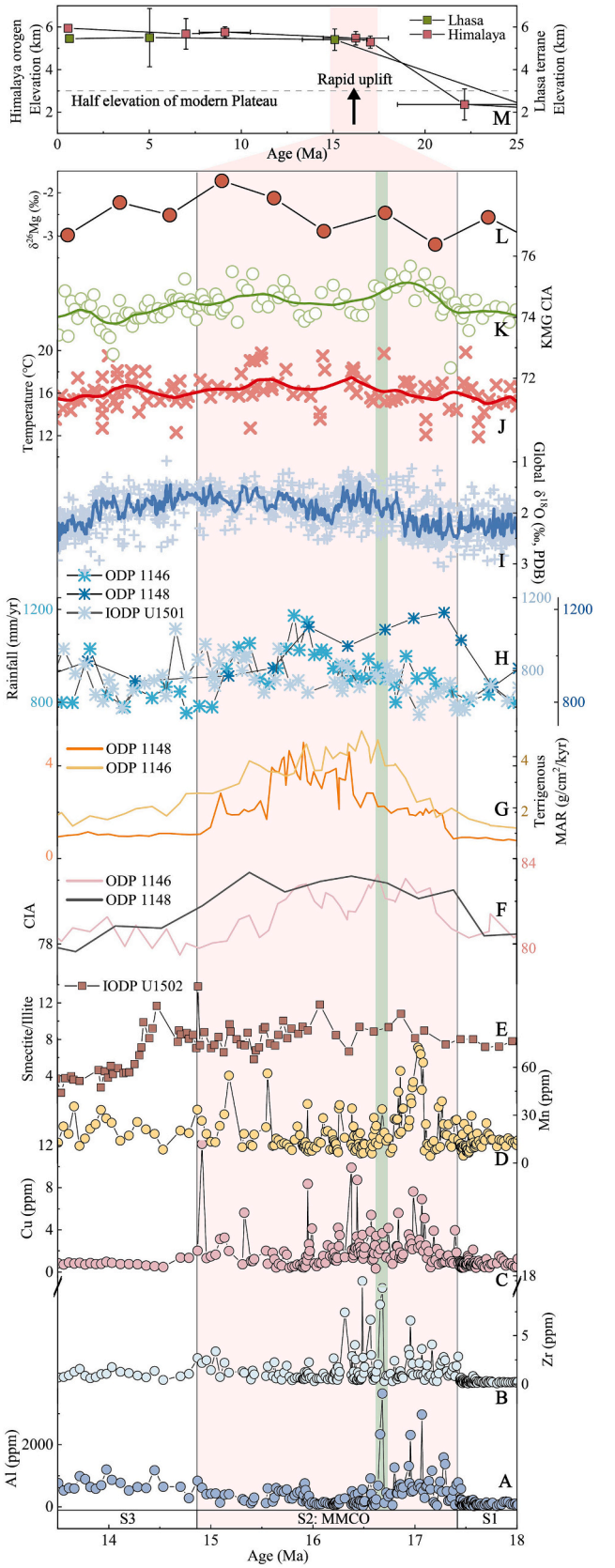

(caption on next column)

Fig. 8. Comparison of elemental records from Well CK2 with regional and global paleoclimatic and paleoenvironmental records. (A-D) Elemental geochemical sequences of Well CK2 in this study, showing the stage-wise evolutionary characteristics of the concentrations of detrital elements (Al and Zr) and seawater environmental indicators (Mn and Cu); (E) Chemical weathering intensity recorded by the smectite/illite ratio at IODP Site U1502 in the northern SCS (He et al., 2022); (F) Chemical Index of Alteration (CIA) values at ODP Sites 1146 and 1148 in the northern SCS (Clift et al., 2014; Wan et al., 2007); (G) Mass accumulation rates (MAR) of terrigenous detritus at ODP Sites 1146 and 1148; (H) Calculated EASM rainfall values inverted from ODP Sites 1146, 1148, and IODP Site U1501 (Wan et al., 2025); (I) Global deep-sea benthic foraminiferal oxygen isotope record (Zachos et al., 2001); (J) Reconstructed global mean temperature sequence for the Miocene (Song et al., 2019); (K) CIA values from the KMG section on the Loess Plateau (Wu et al., 2025); (L) Evolutionary history of EASM precipitation recorded by δ^{26}Mg values from the Zhuanglang section on the Loess Plateau (Ma et al., 2022); (M) Uplift history of the Himalayas and the Tibetan Plateau (Ding et al., 2017; Wan et al., 2025). The pink shaded area indicates stage S2, and the green shaded areas highlight the periods of elevated detrital element concentrations at 16.66 and 16.68 Ma. (For interpretation of the references to colour in this figure legend, the reader is referred to the web version of this article.)

5–6 km by ~17 Ma (Fig. 8M) (Ding et al., 2017; Su et al., 2019), indicating that the major high-topographic framework of Asia had largely been established. This massive plateau profoundly reorganized atmospheric circulation through the pronounced land–sea thermal contrast and orographic dynamic forcing, providing an important topographic basis for the development of a strong EASM (An et al., 2001; Prell and Kutzbach, 1992). The intensified EASM and the associated peak in continental weathering during this period are broadly supported by multiple independent terrestrial and marine records. Regarding marine records, EASM precipitation reconstructions, terrigenous mass accumulation rates (MAR), and chemical index of alteration (CIA) values from sediments at ODP Sites 1146 and 1148 and IODP Site U1501, located to the northeast of the CK2 core site, generally indicate enhanced monsoon precipitation and continental weathering during 17.2–14.7 Ma (Fig. 8F–H; Clift et al., 2014; Wei et al., 2006; Wan et al., 2025). Concurrently, the elevated smectite/illite ratios and illite crystallinity at IODP Site U1502 during the same interval also suggest intensification of chemical weathering around the SCS (Fig. 8E; He et al., 2022). For terrestrial records, the CIA values of red clay from the Kaimengou section (Fig. 8K; Wu et al., 2025) and the δ^{26}Mg record of red clay from the Zhuanglang section (Fig. 8L; Ma et al., 2022) on the Loess Plateau show distinct shifts during the corresponding MMCO interval, likewise indicating intensified hydroclimate and continental chemical weathering. These terrestrial and marine records show a generally consistent stage-wise pattern with the increase in terrigenous input indicators in the CK2 core, indicating a common climatic background for the widespread enhancement of regional terrigenous supply and deposition during the MMCO. Meanwhile, high sediment accumulation rates recorded in Asian basins indicate that tectonic activity and erosional processes on the Tibetan Plateau remained active during the middle Miocene (Wu et al., 2025). Under the globally warm conditions of the MMCO, the established high topography of the plateau strengthened the penetration of the EASM into the continental interior, while continued tectonic activity and erosion continuously generated and exposed fresh weatherable material, together providing favorable conditions for continental weathering in East Asia (Wu et al., 2025). Strong monsoon precipitation further accelerated chemical weathering and physical erosion across South China. Therefore, we suggest that the increased terrigenous material flux during S2 was primarily the result of the strengthened regional weathering and erosion driven by strong EASM during the MMCO, thereby generating more terrigenous material available for aeolian transport. The substantial increase in terrigenous material from the source area provided an abundant supply for aeolian dust transport. Even though the EAWM transport efficiency was not at its maximum during the MMCO, the rich source supply was sufficient to

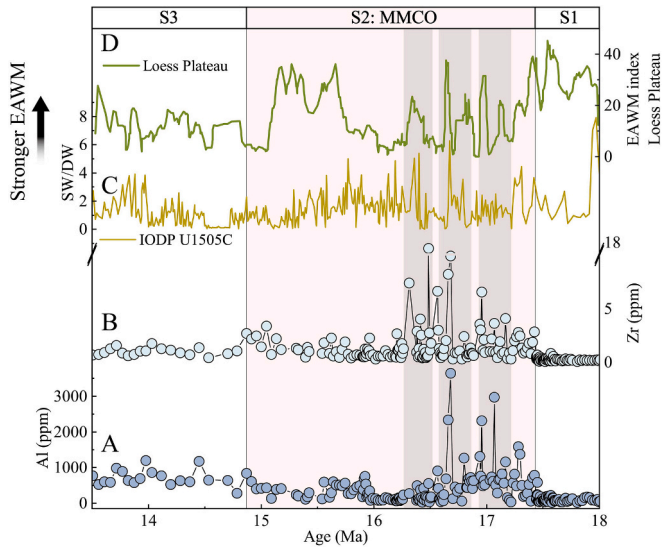

Fig. 9. Comparison between EAWM intensity and Al and Zr concentrations. (A-B) Variations in Al and Zr concentrations; (C) EAWM intensity changes indicated by the Shallow Water species/Deep Water species (SW/DW) ratio of planktonic foraminifera at IODP Site U1505C (Lu et al., 2026); (D) Reconstruction of EAWM variations based on the grain-size end-member model from the Loess Plateau (Jiang et al., 2017). The pink shaded area indicates stage S2, and the grey shaded areas highlight intervals of elevated EAWM intensity and high Al and Zr concentrations during early S2. (For interpretation of the references to colour in this figure legend, the reader is referred to the web version of this article.)

drive a significant rise in aeolian dust fluxes to the Xisha platform. Conversely, the relatively low aeolian dust input during stage S1 was likely due to the weaker EASM, which led to an insufficient supply of terrigenous material in the source area. Consequently, despite a stronger EAWM transport capacity, there was a lack of adequate terrigenous material for long-distance transport, resulting in overall low concentrations of Al, Ti, and Zr. Notably, the synchronous pronounced peaks of the three proxies at 16.66 and 16.68 Ma, as mentioned in Section 5.1, occur within an interval characterized by elevated MMCO temperatures, continental weathering intensity, EASM precipitation, and EAWM strength (Figs. 3, 8, 9). These anomalies may reflect an extreme response to both the robust EASM-driven continental weathering and erosion during the warm period and the intense EAWM transport mechanism.

The above interpretation is further supported by the Sr isotope data from Well CK2. Anomalously elevated $^{87}Sr/^{86}Sr$ values exceeding the Sr isotope chronologic framework have also been documented in the upper Pleistocene section of Well CK2, where they were attributed to enhanced terrigenous influence (Jiang et al., 2019). In this study, similar $^{87}Sr/^{86}Sr$ anomalies are observed and predominantly concentrated in S2 (Fig. 2). In particular, during the interval of approximately 16.6–16.0 Ma, the anomalously high $^{87}Sr/^{86}Sr$ values broadly coincide temporally with the elevated terrigenous detrital input indicated by Al, Ti, and Zr (Fig. 3, S2). Previous studies attributed the $^{87}Sr/^{86}Sr$ anomalies in this interval to meteoric alteration of carbonates during periods of sea-level fall (Yang et al., 2022). However, typical meteoric alteration should be accompanied by synchronous extreme negative excursions in both $\delta^{13}C$ and $\delta^{18}O$ and a significant increase in Mn/Sr. The data show that these indicators do not exhibit pronounced alteration signatures in the relevant interval (Fig. S1). Moreover, not only are Al, Ti, and Zr elevated in this interval, but Mn, Ni, and Cu also increase simultaneously (Fig. S2). The concurrent response of these two independent element groups is difficult to explain by selective enrichment from weathering residues on exposure surfaces, and instead is more consistent with the superposition of enhanced terrigenous input and elevated marine productivity during the MMCO. Given that the $^{87}Sr/^{86}Sr$ ratios of silicate components in

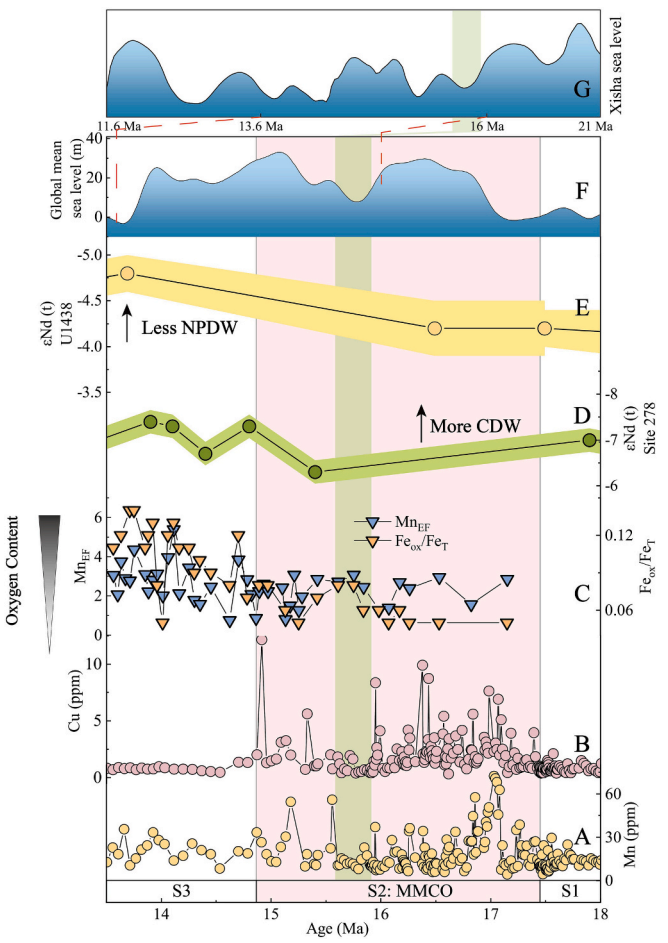

Fig. 10. Evolution of trace elements in Well CK2 and comparison with regional oceanographic and sea-level records. (A-B) Evolutionary characteristics of the concentrations of redox- and paleoproductivity-sensitive trace elements (Mn and Cu) in carbonates from Well CK2; (C) Gradient changes in bottom-water oxygenation inverted from Mn_{EF} and Fe_{ox}/Fe_T at ODP Site 1146 (Zhang et al., 2025); (D) Intensity variations of Circumpolar Deep Water (CDW) indicated by the εNd record of fossil fish bone debris at DSDP Site 278 (Evangelinos et al., 2024); (E) Activity intensity of North Pacific Deep Water (NPDW) indicated by the εNd record of fossil fish teeth and Fe-Mn coatings at IODP Site 1438 (Kender et al., 2018); (F) Global mean sea-level fluctuation curve (Miller et al., 2020); (G) Evolutionary history of regional sea level in the Xisha area (Shao et al., 2017a). The green shaded area indicates an exposure surface identified at ~15.9 Ma in Well CK2, corresponding to a brief drop in global and Xisha sea-level records. (For interpretation of the references to colour in this figure legend, the reader is referred to the web version of this article.)

Miocene aeolian dust from the Chinese Loess Plateau can reach 0.716–0.720 (Chen and Li, 2013), far exceeding contemporaneous seawater values (~0.7087), isotopic exchange with radiogenic Sr hosted in siliciclastic detrital components may have produced the positive shift in carbonate $^{87}Sr/^{86}Sr$. At Well XK-1, also located in the Xisha Islands, the Al/Sr ratios (Shao et al., 2017a) and $^{87}Sr/^{86}Sr$ values (Bi et al., 2019) from the corresponding interval (approximately 1030–1060 m depth) display a similar increasing trend (Fig. S2F–G). This implies that the Xisha carbonate platform may have been broadly affected by enhanced terrigenous material input during this period. It should be noted, however, that Well XK-1 has only three age control points (21.0, 16.0, and 13.6 Ma) within the studied time window, resulting in limited chronostratigraphic resolution. Therefore, the precision of this event correlation requires further verification through higher-resolution geochronological work. Therefore, we propose that the anomalously elevated $^{87}Sr/^{86}Sr$ values during S2 in Well CK2 cannot be attributed

entirely to meteoric alteration. The multi-proxy covariation of Al, Ti, Zr, and $^{87}Sr/^{86}Sr$ during S2 indicates that highly radiogenic Sr carried by terrigenous aeolian dust during the MMCO modified the Sr isotopic composition of the carbonates to a certain extent.

The coordinated pattern of synchronous variation in Al, Ti, and Zr during S2 broke down in S3, with Al continuing to increase while Ti and Zr declined substantially. During this period (after ~15 Ma), declining atmospheric CO_2 concentrations and global cooling became increasingly important controls on EASM precipitation (Wan et al., 2025). Under the cold and arid climatic regime of the MMCT, the retreat of the EASM led to a sharp reduction in precipitation, and continental chemical weathering and physical erosion weakened overall. This not only suppressed the release of loose detrital from parent rocks at the source but also significantly reduced the total volume of terrigenous material delivered to the marginal seas. Given the overall contraction in source area detrital supply, a possible mechanism for the elemental decoupling observed during S3 is a change in the mineral composition of the terrigenous detritus reaching Well CK2. Generally, Al is predominantly hosted in fine-grained aluminosilicate clay minerals (Li et al., 2020; Rimmer, 2004; Zhou et al., 2023a). Zr exists almost entirely in the form of zircon; the occurrence of Ti is more complex, as it can be hosted in heavy minerals such as rutile (TiO_2) or partially incorporated into the clay mineral lattice (Calvert and Pedersen, 2007; Govin et al., 2012; Kidder and Erwin, 2001; Zhou et al., 2023b). The elemental correlation analysis for stage S3 in this study confirms this material distribution pattern. Al shows a strong positive correlation with Si ($r = 0.77$, $p < 0.01$), indicating that both are co-hosted in terrigenous aluminosilicate clay minerals. The moderate correlation between Ti and Si ($r = 0.54$, $p < 0.05$) reflects the mixed occurrence of Ti in both clay and heavy minerals, whereas Zr exhibits almost no correlation with Si ($r = 0.31$, $p > 0.5$), demonstrating that variations in Zr concentrations are independent of the clay mineral component (Calvert and Pedersen, 2007; Govin et al., 2012). The characteristic pattern of elevated Al but low Ti and Zr during S3 therefore suggests that the terrigenous detritus reaching the carbonate platform were dominated by fine-grained clay minerals, with a relative paucity of heavy mineral components. This is because, under conditions dominated by long-distance transport, the grain-size and density sorting effects on detritus become particularly significant: clay minerals, being fine-grained and low in density, are readily transported over long distances, whereas heavy minerals, with their higher density, have transport efficiencies far lower than those of clay minerals (Lawrence and Neff, 2009; Rea, 1994). The isolated position of Well CK2, far from the continent, further amplifies this sorting effect. Superimposed on the climatic background where the EAWM did not experience a drastic intensification during S3 (Fig. 9), the dynamic conditions for transporting heavy minerals to the Xisha waters were limited, ultimately leading to the decoupling of indicator elements for light and heavy minerals during this stage.

6.2. Evolution of paleoproductivity conditions

Primary productivity on carbonate platforms is largely dependent on the supply of nutrients. For isolated platforms far from the continent, upwelling and terrigenous input are generally the main sources of nutrients to surface waters (Betzler et al., 2018; Jiang et al., 2019; Ortega-Ariza et al., 2021; Torfstein and Steinberg, 2020). As previously mentioned, the Xisha Islands lack any direct nutrient input from terrestrial rivers. Furthermore, no correlation exists between productivity proxies and terrigenous input indicators. This suggests that the increase in micronutrients driving enhanced productivity was not derived from terrigenous material input but was primarily controlled by upwelling (Jiang et al., 2019; Liu et al., 2023; Wu et al., 2019b; Zhu et al., 2022). The EASM-driven coastal upwelling originates along the eastern coast of Vietnam and is still well developed in the waters southwest of the Xisha Islands at present (Xie et al., 2003). This monsoon-driven upwelling likely extended to the Xisha Islands from the late Early Miocene to the Middle Miocene (Clift et al., 2014; Wu et al., 2019b). The intensification of monsoonal winds can promote surface Ekman transport and accelerate the upwelling of deep, nutrient-rich waters to the surface. In addition, sea-level evolution also is a key factor constraining the extent and intensity of upwelling (Ortega-Ariza et al., 2021; Shao et al., 2017a; Zhao et al., 2026). During sea-level rise, shallow-water carbonate platforms are transformed into open marine environments, vertical seawater exchange and nutrient transport are enhanced, and regional upwelling intensifies, thereby increasing marine primary productivity (Ortega-Ariza et al., 2021; Zhao et al., 2026). A transient sea-level fluctuation event within S2 provides further support for this mechanism. An exposure surface identified at ~15.9 Ma in Well CK2 broadly corresponds to a brief fall recorded in both global and Xisha sea-level records (Fig. 10). The concentrations of Ni, Cu, and Mn concurrently show distinct troughs during this period, and subsequently recover rapidly to the high levels of stage S2 as sea level rises again (Fig. 10). This phenomenon indicates that the brief sea-level fall caused an interruption in the carbonate platform depositional environment, leaving a discernible signal in the trace element record.

Based on the above mechanisms, the primary productivity evolution recorded in Well CK2 displays pronounced stage-wise characteristics. During S1, Ni and Cu concentrations remained at relatively low levels overall. The East Asian monsoon had not yet fully developed during this period, the contribution of wind-driven upwelling was limited, and the platform was generally in an oligotrophic state with insufficient nutrient flux. Upon entering S2, Ni and Cu concentrations increased significantly relative to S1, marking the establishment of a high-productivity environment. During the MMCO, global warming and the retreat of the Antarctic ice sheet triggered a substantial sea-level rise (Fielding et al., 2011; Miller et al., 2020; Warny et al., 2009). The rise in both global and regional relative sea level significantly increased the accommodation space and water depth over the carbonate platforms of the Nansha and Xisha Islands (Su et al., 2024). At this point, the increased water depth was accompanied by a landward migration and intensification of upwelling (Ortega-Ariza et al., 2021). Simultaneously, the significant strengthening of the EASM during the MMCO further promoted the transport of deep, nutrient-rich waters to the surface through wind-driven upwelling. Furthermore, the intensification of oceanic circulation may also have enhanced upwelling to some extent, thereby promoting surface primary productivity (Cornacchia et al., 2021). The εNd record from IODP Site U1438 indicates enhanced formation of North Pacific Deep Water (NPDW) during the MMCO (Fig. 10E). NPDW may have overflowed into the deep basin of the SCS through the Luzon Strait and transported nutrients upward to the mid-upper water column through diapycnal mixing (Zhang et al., 2025; Zhou et al., 2023a; Zhou et al., 2017). However, NPDW primarily affected the deep to intermediate-depth waters of the SCS, and considerable uncertainty remains as to whether the nutrients it carried could have been efficiently transported to the upper waters of the shallow Xisha carbonate platform. In comparison, sea-level rise and EASM-driven upwelling were likely more direct and important mechanisms for nutrient supply. Although terrestrial runoff was clearly not the primary controlling factor, long-term terrigenous input to the SCS may still have provided a supplementary regional source of nutrient. The enhanced continental chemical weathering and erosion during the MMCO may also have delivered nutrient elements (e.g., P, Fe) to the marginal seas via terrigenous pathways (Bao et al., 2019; Clift et al., 2014; Holbourn et al., 2021; Zhang et al., 2025). These processes collectively drove a burst of marine primary productivity in the SCS. For example, Site LF14 in the Lufeng Sag of the northern SCS also recorded peak total organic carbon contents during ~17.5–14.7 Ma (Xue et al., 2019), and the rapid reef construction at Well NK-1 on Mischief Reef in the Nansha Islands during 18–13.5 Ma has likewise been attributed to a major bloom in biological productivity under conditions of enhanced weathering and precipitation (Su et al., 2024). Based on the relatively low local contents of algal boundstonesat at Well XK-1 on Shidao Island, Wu et al. (2019b) inferred

a lack of EASM and upwelling during 17.3–15.5 Ma. However, this inference starkly contradicts a wide range of current regional paleoenvironmental records. The multiple independent proxy indicators compiled in this study (Fig. 8) consistently point to the EASM being at its peak intensity during the MMCO, which is in agreement with the elevated trace element concentrations in Well CK2. Beyond the geochemical indicators, changes in paleobiotic assemblages also point to fluctuations in environmental nutrient levels. In the 760–560 m interval of Well CK2 (approximately 17.42–14.87 Ma), heterotrophic faunal communities represented by bryozoans, mollusks, planktonic foraminifera, and miliolids underwent a significant proliferation (see Fig. 5 of Meng et al., 2022). In tropical settings, such a phenomenon is typically associated with mesotrophic to eutrophic conditions (Coletti et al., 2017; Halfar et al., 2004; Ortega-Ariza et al., 2021). During the same interval, the transition from coral-dominated to red algae-dominated assemblages is also related to increased nutrient supply (e.g., Halfar and Mutti, 2005; Hallock and Schlager, 1986; Wu et al., 2019a), consistent with the elevated water-column nutrient levels indicated by Ni and Cu.

With the climate transition, Ni and Cu concentrations declined to their lowest levels across all three stages during S3, indicating a sharp decline in platform primary productivity. During the MMCT, global climate cooling and the expansion of the Antarctic ice sheet led to significant falls in both global and Xisha sea levels (Miller et al., 2020; Shao et al., 2017a). The sea-level decline caused upwelling to retreat seaward and weaken in intensity (e.g., Ortega-Ariza et al., 2021), reducing the efficiency of nutrient delivery to the platform. Furthermore, the weakened EASM during the MMCT reduced the intensity of wind-driven upwelling, further limiting the efficiency of vertical nutrient transport. Climate cooling also led to diminished continental chemical weathering and erosion, thereby reducing riverine nutrient input (Clift et al., 2014; Holbourn et al., 2021), further diminishing the nutrient foundation for marine productivity via the terrigenous pathway.

The $\delta^{13}C$ record of carbonates from Well CK2 provides supplementary evidence for the three-stage productivity evolution described above. Previous studies on the Pleistocene section of the same well have demonstrated that the $\delta^{13}C$ of Xisha coral reef carbonates can, to a certain extent, reflect variations in seawater $\delta^{13}C$ and regional carbon cycling (Xu et al., 2019). In this study, the stage-wise changes in $\delta^{13}C$ are broadly consistent with the productivity evolution indicated by Ni and Cu: $\delta^{13}C$ values are overall more positive during S2, synchronous with the increase in Ni and Cu, and shift toward more negative values during S3, synchronous with the decline in Ni and Cu (Fig. 11). It should be noted that an extreme negative excursion in $\delta^{13}C$ (as low as approximately −4‰) occurs near the exposure surface identified at 15.9 Ma. This anomaly has no counterpart in other global or regional records and is accompanied by a synchronous negative excursion in $\delta^{18}O$, likely reflecting localized meteoric diagenetic alteration. This interval is therefore excluded from the trend comparison. The long-term $\delta^{13}C$ trend of Well CK2 is comparable to those from Mediterranean shallow-water carbonate platforms (Latium Abruzzi Pietrasecca, S. Bartolomeo/Orta Majella) (Brandano et al., 2017), the benthic foraminiferal $\delta^{13}C$ record from ODP Site 1148 (Zhao et al., 2001), and the Δ_p record from ODP Site 1148 (Jia et al., 2003). All these records reach relatively high values between ~16.5–15.5 Ma and gradually decrease thereafter (Fig. 11), implying that Well CK2 preserves the primary signal of the global Middle Miocene carbon isotope positive excursion event. Superimposed on the global signal, regional factors may have further modulated the $\delta^{13}C$ record of Well CK2. The enhanced upwelling and increased terrigenous nutrient input during the MMCO elevated regional productivity, consistent with the synchronous increases in Ni, Cu, and Al, Ti, Zr. Meanwhile, the Δ_p record from ODP Site 1148 indicates that C_3 vegetation cover on the East Asian continent was significantly higher during this period (Jia et al., 2003), pointing to warm and humid climatic conditions. C3 plants exhibit much stronger fractionation of ^{13}C during photosynthesis than C4 plants. Terrestrial ecosystems dominated by C3

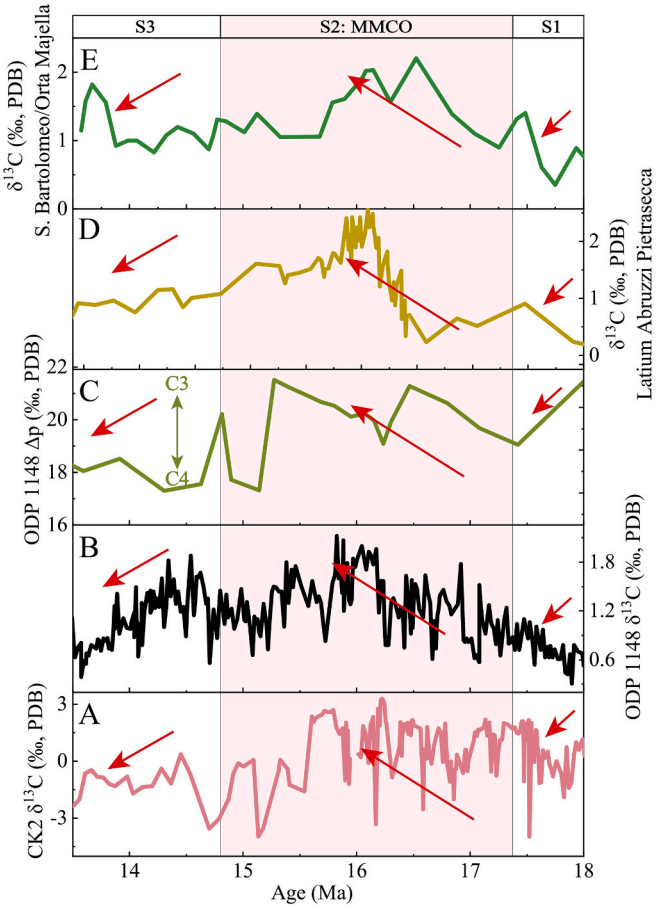

Fig. 11. Comparison of the $\delta^{13}C$ record of Well CK2 with global and regional carbon isotope records. (A) Whole-rock carbonate $\delta^{13}C$ record of Well CK2; (B) Benthic foraminiferal $\delta^{13}C$ record at ODP Site 1148 (Zhao et al., 2001); (C) Δ_p record at ODP Site 1148 (i.e., the difference between atmospheric $\delta^{13}C$ and black carbon $\delta^{13}C$, indicating the evolution of C3/C4 vegetation on the East Asian landmass) (Jia et al., 2003); (D-E) $\delta^{13}C$ records from the S. Bartolomeo/Orta Majella section and the Pietrasecca section of the Latium-Abruzzi carbonate platform in the central Mediterranean (Brandano et al., 2017).

vegetation sequester more light carbon (^{12}C) in their biomass, potentially causing a relatively positive shift in the $\delta^{13}C$ of concurrent seawater dissolved inorganic carbon (Jia et al., 2003). The overall positive $\delta^{13}C$ values at Well CK2 during S2 are consistent with this mechanism, echoing the covariation between CK2 $\delta^{13}C$ and the East Asian terrestrial ecosystem observed by Xu et al. (2019) in the Pleistocene section of the same well. However, the whole-rock $\delta^{13}C$ of Well CK2 is controlled by multiple factors, including differences in $\delta^{13}C$ among different biotic components (corals, coralline algae, foraminifera, etc.) and variations in their relative proportions (Brandano et al., 2017; Weber and Woodhead, 1969), metabolic fractionation effects in coral skeletons (McConnaughey, 1989; Swart, 1983), and diagenetic alteration (as reflected by the positive correlation between $\delta^{13}C$ and $\delta^{18}O$, $r = 0.74$, $p < 0.01$). These local effects result in a $\delta^{13}C$ amplitude at Well CK2 (approximately −4‰ to +3‰) that is far greater than those of contemporaneous pelagic and shallow-water carbonate platform records, making it difficult to effectively separate the global signal from local noise. Therefore, this study uses the stage-wise $\delta^{13}C$ trends only as supplementary evidence for productivity evolution.

6.3. Evolution of paleoredox conditions

Mn concentrations in carbonates are highly sensitive to the redox conditions of the regional depositional environment and have been

widely used to trace suboxic rather than fully anoxic conditions in shallow-water carbonate depositional settings, serving as an effective proxy for reconstructing paleoredox states (Jenkyns et al., 1991; Wittkop et al., 2020). It should be noted that this study does not perform quantitative evaluations based on specific thresholds. Instead, it focuses on the overall variation trends of Mn concentrations to explore the stage-wise evolution of the redox state of the depositional water column.

Marine redox conditions are typically co-constrained by factors such as the dissolved oxygen capacity of the water column, oxygen consumption by organic matter respiration, and ocean circulation ventilation (Hoogakker et al., 2025; Keeling et al., 2010; Levin, 2018; Zhang et al., 2025). During S1, Mn concentrations were at their lowest across all three stages, indicating that the depositional water column was characterized by relatively oxic conditions. This is consistent with the expectation that, under the low-productivity background of this period, the organic matter settling flux was limited and oxygen consumption through organic matter mineralization was correspondingly low. Under oxygenated bottom-water conditions, Mn exists predominantly as Mn^{3+}/Mn^{4+} oxides/hydroxides, whereas when the water column becomes suboxic to anoxic, previously deposited Mn oxides/hydroxides are reduced to soluble Mn^{2+}, which is subsequently enriched in the crystal lattice of early diagenetic carbonates (Huckriede and Meischner, 1996; Jenkyns et al., 1991). Upon entering S2, Mn concentrations increased significantly relative to S1, indicating the intensification of suboxic/hypoxic conditions in the bottom waters. One possible mechanism is that the extreme high temperatures of the MMCO significantly reduced the dissolved oxygen saturation capacity of the water column (e.g., Keeling et al., 2010). Another possible mechanism is that the elevated productivity driven by enhanced upwelling led to an increase in the organic matter settling flux, and the degradation of this organic matter consumed substantial amounts of dissolved oxygen, promoting the development of suboxic conditions. The high productivity driven by intense upwelling during S2 may have caused large quantities of organic matter to settle and become buried within the platform sediments. When the organic matter settling flux is sufficiently large, dissolved oxygen in the sediment pore waters can be rapidly depleted. This leads to the reduction of Mn oxides/hydroxides as alternative electron acceptors, releasing soluble Mn^{2+} (Froelich et al., 1979) and thereby promoting the massive enrichment of Mn^{2+} in carbonate minerals.

Mn concentrations during S3 remained at levels comparable to those of S2. The apparent contradiction between the sharp decline in productivity indicators and the persistently elevated Mn values suggests that the maintenance of suboxic conditions during S3 was not driven by high productivity-related oxygen consumption. During the MMCT, both global and Xisha sea levels declined (Fig. 10F–G) (Miller et al., 2020; Shao et al., 2017a). Consequently, the platform water depth became shallower, reef-margin channels likely narrowed, and water circulation between the platform interior and the external open ocean became restricted (Kendall and Schlager, 1981; Zhao et al., 2026). Under such relatively restricted water conditions, even though the substantial decline in productivity during S3 reduced the organic matter settling flux, the degradation of limited organic matter may still have been sufficient to deplete dissolved oxygen to suboxic levels, allowing Mn^{2+} to continue accumulating in the carbonates. A similar phenomenon, in which sea-level fall leads to the development of suboxic to anoxic conditions in carbonate platform bottom waters, has also been documented on the Maldives platform (Swart et al., 2019). The reorganization of oceanic circulation during the MMCT may have partly modulated the regional oxygenation background of the SCS. As NPDW gradually weakened or even disappeared, the upper water column of the North Pacific became occupied by oxygen-depleted North Pacific Intermediate Water (NPIW) (Zhang et al., 2025). Meanwhile, the intensification of Circumpolar Deep Water (CDW) improved deep-water ventilation in the SCS (Zhang et al., 2025), but this improvement in deep-water oxygenation was unlikely to have been directly transmitted to the shallow platform environment. The trend toward enhanced deep water oxygenation recorded by Mn_{EF} and Fe_{ox}/Fe_T at ODP Site 1146 (Zhang et al., 2025; Fig. 10C) contrasts sharply with the persistently high Mn concentrations in Well CK2, suggesting that redox evolution in the shallow-water platform and deep-sea basin may have been controlled by different mechanisms. Notably, Xue et al. (2019) reconstructed variations in water oxygenation based on the foraminiferal record from Well LF14 in the Lufeng Sag, northern SCS, which exhibit stage-wise characteristics: oxygenation was relatively low between 18.7 and 17.54 Ma, further decreased between 17.54 and 14.66 Ma due to elevated productivity, and gradually recovered after 14.66 Ma. The evolutionary trend of the Mn record in Well CK2 is generally consistent with this regional record, indicating that the paleoredox signals captured by trace elements in the carbonate platform reflect a shared response of the shallow to intermediate-deep water environments of the northern SCS to climatic and oceanographic changes from the MMCO to the MMCT.

7. Conclusions

Major and trace element analyses of carbonates from Well CK2 reveal that terrigenous input, marine productivity, and water-column redox conditions on the isolated Xisha carbonate platform underwent significant stage-wise evolution during the MMCO to MMCT. During S1 (~18–17.42 Ma), prior to the MMCO, the EASM was relatively weak, limiting weathering and erosion and reducing terrigenous material supply in the source area. Consequently, terrigenous detrital input (Al, Ti, Zr), productivity indicators (Ni, Cu), and redox indicators (Mn) all remained at low levels, with the platform characterized by an overall oligotrophic and oxic stable environment. During the MMCO (S2: ~17.42–14.87 Ma), strengthened EASM precipitation promoted continental chemical weathering and physical erosion. These processes generated abundant terrigenous material that reached the Xisha platform via aeolian dust deposition, leading to a marked increase in terrigenous detrital fluxes. The anomalously elevated $^{87}Sr/^{86}Sr$ values concentrated in this stage further support enhanced terrigenous input, as radiogenic Sr carried by aeolian siliciclastic material modified the carbonate Sr isotopic composition. Simultaneously, the synergistic effects of high sea level and strong monsoon-driven upwelling promoted a massive burst in platform productivity. This process is also supported by the overall positive shift in the $\delta^{13}C$ record during this period. The oxygen consumption by organic matter resulting from the high productivity created local suboxic conditions within the platform, subsequently causing the enrichment of Mn^{2+} in the carbonates. During the subsequent MMCT (S3: ~14.87–13.5 Ma), the weakening of the EASM led to a decrease in the total amount of terrigenous material supplied from source area. The sorting effects of grain size and density during long-distance aeolian dust transport allowed Al to remain at high levels while Ti and Zr declined substantially. Sea-level fall and the weakening of monsoon-driven upwelling collectively caused a sharp decline in productivity, accompanied by a negative shift in $\delta^{13}C$. Despite the substantial decline in productivity, Mn remained high. This indicates that the dominant mechanism shifted from the oxygen consumption process triggered by high productivity in stage S2, to the restricted water circulation caused by sea-level fall in stage S3.

CRediT authorship contribution statement

Ning Guo: Writing – original draft, Visualization, Software, Investigation, Formal analysis. **Wei Jiang:** Writing – review & editing, Visualization, Supervision, Methodology, Investigation, Formal analysis, Conceptualization. **Tianlai Fan:** Investigation, Data curation. **Shendong Xu:** Investigation, Data curation. **Rui Wang:** Investigation, Data curation. **Jian-xin Zhao:** Methodology, Data curation. **Yue-xing Feng:** Methodology, Data curation. **Kefu Yu:** Visualization, Supervision, Resources, Project administration, Funding acquisition.

Declaration of competing interest

The authors declare that they have no known competing financial interests or personal relationships that could have appeared to influence the work reported in this paper.

Acknowledgements

This work was financially supported by the National Natural Science Foundation of China (Grant Nos. 42030502), the Guangxi Science and Technology Program (No. AD25069075), the Major Talent Project of Guangxi Zhuang Autonomous Region (GXR-1BGQ2424020), and the Innovation Project of Guangxi Graduate Education (YCSW2024062).

Appendix A. Supplementary data

Supplementary data to this article can be found online at https://doi.org/10.1016/j.palaeo.2026.114182.

Data availability

All data used in this study are provided in the Supplementary Materials.

Paleoenvironmental response in the South China Sea from the Middle Miocene Climatic Optimum to the Middle Miocene Climate Transition: Geochemical records from an isolated carbonate platform (Figshare)

References

Algeo, T.J., Twitchett, R.J., 2010. Anomalous Early Triassic sediment fluxes due to elevated weathering rates and their biological consequences. Geology 38, 1023–1026. https://doi.org/10.1130/G31203.1.

Alibo, D.S., Nozaki, Y., 2000. Dissolved rare earth elements in the South China Sea: geochemical characterization of the water masses. J. Geophys. Res. Oceans 105, 28771–28783. https://doi.org/10.1029/1999JC000283.

An, Z., Kutzbach, J.E., Prell, W.L., Porter, S.C., 2001. Evolution of Asian monsoons and phased uplift of the Himalaya–Tibetan plateau since late Miocene times. Nature 411, 62–66. https://doi.org/10.1038/35075035.

Arnaboldi, M., Meyers, P.A., 2007. Trace element indicators of increased primary production and decreased water-column ventilation during deposition of latest Pliocene sapropels at five locations across the Mediterranean Sea. Palaeogeogr. Palaeoclimatol. Palaeoecol. 249, 425–443. https://doi.org/10.1016/j.palaeo.2007.02.016.

Ashok, M., Absar, N., 2025. Carbon cycling, redox condition and solute fluxes in the middle Paleoproterozoic Ocean: constraints from elemental and C-O, Nd-Sr isotope geochemistry of stromatolitic carbonates from Vempalle Formation, Cuddapah Basin. Precambrian Res. 419, 107724. https://doi.org/10.1016/j.precamres.2025.107724.

Azmy, K., Brand, U., Sylvester, P., Gleeson, S.A., Logan, A., Bitner, M.A., 2011. Biogenic and abiogenic low-Mg calcite (bLMC and aLMC): evaluation of seawater-REE composition, water masses and carbonate diagenesis. Chem. Geol. 280, 180–190. https://doi.org/10.1016/j.chemgeo.2010.11.007.

Banner, J.L., Hanson, G.N., 1990. Calculation of simultaneous isotopic and trace element variations during water-rock interaction with applications to carbonate diagenesis. Geochim. Cosmochim. Acta 54, 3123–3137. https://doi.org/10.1016/0016-7037(90)90128-8.

Bao, R., Jia, G., Zhang, C., 2019. Spatiotemporal variation of organic geochemical properties since the mid-Miocene in the deep South China Sea (IODP Expedition 349). J. Asian Earth Sci. 183, 103961. https://doi.org/10.1016/j.jseaes.2019.103961.

Betzler, C., Eberli, G.P., Lüdmann, T., Reolid, J., Kroon, D., Reijmer, J.J.G., Swart, P.K., Wright, J., Young, J.R., Alvarez-Zarikian, C., Alonso-García, M., Bialik, O.M., Blättler, C.L., Guo, J.A., Haffen, S., Horozal, S., Inoue, M., Jovane, L., Lanci, L., Laya, J.C., Hui Mee, A.L., Nakakuni, M., Nath, B.N., Niino, K., Petruny, L.M., Pratiwi, S.D., Slagle, A.L., Sloss, C.R., Su, X., Yao, Z., 2018. Refinement of Miocene Sea level and monsoon events from the sedimentary archive of the Maldives (Indian Ocean). Prog Earth Planet Sci. 5, 5. https://doi.org/10.1186/s40645-018-0165-x.

Bi, D., Zhang, D., Zhai, S., Liu, Xinyu, Xiu, C., Liu, Xiaofeng, Jiang, L., Zhang, A., 2019. Seawater $^{87}Sr/^{86}Sr$ values recorded by reef carbonates from the Xisha Islands (South China Sea) since the Neogene and its response to the uplift of Qinghai-Tibetan Plateau. Geol. J. 54, 3878–3890. https://doi.org/10.1002/gj.3386.

Bottini, C., Cohen, A.S., Erba, E., Jenkyns, H.C., Coe, A.L., 2012. Osmium-isotope evidence for volcanism, weathering, and ocean mixing during the early Aptian OAE 1a. Geology 40, 583–586. https://doi.org/10.1130/G33140.1.

Brand, U., Veizer, J., 1980. Chemical diagenesis of a multicomponent carbonate system–1: trace elements. J. Sediment. Res. 50, 1219–1236. https://doi.org/10.1306/212F7BB7-2B24-11D7-8648000102C1865D.

Brandano, M., Cornacchia, I., Raffi, I., Tomassetti, L., Agostini, S., 2017. The Monterey Event within the Central Mediterranean area: the shallow-water record. Sedimentology 64, 286–310. https://doi.org/10.1111/sed.12348.

Calvert, S.E., Pedersen, T.F., 2007. Chapter Fourteen elemental proxies for palaeoclimatic and palaeoceanographic variability in marine sediments: interpretation and application. In: Developments in Marine Geology. Elsevier, pp. 567–644. https://doi.org/10.1016/S1572-5480(07)01019-6.

Camoin, G.F., Webster, J.M., 2015. Coral reef response to Quaternary Sea-level and environmental changes: state of the science. Sedimentology 62, 401–428. https://doi.org/10.1111/sed.12184.

Chen, Z., Li, G., 2013. Evolving sources of Eolian detritus on the Chinese Loess Plateau since early Miocene: tectonic and climatic controls. Earth Planet. Sci. Lett. 371, 220–225. https://doi.org/10.1016/j.epsl.2013.03.044.

Chen, X., Zhang, F., Lin, Y., Cao, M., Wei, H., Xu, C., Fan, C., Shen, S., 2024. Boron isotopic compositions of middle Miocene to recent shallow-water carbonates from the South China Sea: assessing diagenetic effects and implications for paleoclimate changes. Glob. Planet. Chang. 240, 104511. https://doi.org/10.1016/j.gloplacha.2024.104511.

Clift, P.D., Wan, S., Blusztajn, J., 2014. Reconstructing chemical weathering, physical erosion and monsoon intensity since 25 Ma in the northern South China Sea: a review of competing proxies. Earth Sci. Rev. 130, 86–102. https://doi.org/10.1016/j.earscirev.2014.01.002.

Coletti, G., El Kateb, A., Basso, D., Cavallo, A., Spezzaferri, S., 2017. Nutrient influence on fossil carbonate factories: evidence from SEDEX extractions on Burdigalian limestones (Miocene, NW Italy and S France). Palaeogeogr. Palaeoclimatol. Palaeoecol. 475, 80–92. https://doi.org/10.1016/j.palaeo. 2017.03.005.

Cornacchia, I., Munnecke, A., Brandano, M., 2021. The potential of carbonate ramps to record C-isotope shifts: insights from the upper Miocene of the Central Mediterranean area. Lethaia 54, 73–89. https://doi.org/10.1111/let.12383.

Derry, L.A., 2010. A burial diagenesis origin for the Ediacaran Shuram–Wonoka carbon isotope anomaly. Earth Planet. Sci. Lett. 294, 152–162. https://doi.org/10.1016/j.epsl.2010.03.022.

Ding, L., Spicer, R.A., Yang, J., Xu, Q., Cai, F., Li, S., Lai, Q., Wang, H., Spicer, T.E.V., Yue, Y., Shukla, A., Srivastava, G., Khan, M.A., Bera, S., Mehrotra, R., 2017. Quantifying the rise of the Himalaya orogen and implications for the South Asian monsoon. Geology 45, 215–218. https://doi.org/10.1130/G38583.1.

Duda, J.-P., Blumenberg, M., Thiel, V., Simon, K., Zhu, M., Reitner, J., 2014. Geobiology of a palaeoecosystem with Ediacara-type fossils: the Shibantan Member (Dengying Formation, South China). Precambrian Res. 255, 48–62. https://doi.org/10.1016/j.precamres.2014.09.012.

Evangelinos, D., Etourneau, J., van de Flierdt, T., Crosta, X., Jeandel, C., Flores, J.-A., Harwood, D.M., Valero, L., Ducassou, E., Sauermilch, I., Klocker, A., Cacho, I., Pena, L.D., Kreissig, K., Benoit, M., Belhadj, M., Paredes, E., Garcia-Solsona, E., López-Quirós, A., Salabarnada, A., Escutia, C., 2024. Late Miocene onset of the modern Antarctic circumpolar current. Nat. Geosci. 17, 165–170. https://doi.org/10.1038/s41561-023-01356-3.

Fan, T., Yu, K., Zhao, J., Jiang, W., Xu, S., Zhang, Y., Wang, R., Wang, Y., Feng, Y., Bian, L., Qian, H., Liao, W., 2020. Strontium isotope stratigraphy and paleomagnetic age constraints on the evolution history of coral reef islands, northern South China Sea. Geol. Soc. Am. Bull. 132, 803–816. https://doi.org/10.1130/B35088.1.

Fielding, C.R., Browne, G.H., Field, B., Florindo, F., Harwood, D.M., Krissek, L.A., Levy, R.H., Panter, K.S., Passchier, S., Pekar, S.F., 2011. Sequence stratigraphy of the ANDRILL AND-2A drillcore, Antarctica: a long-term, ice-proximal record of Early to Mid-Miocene climate, sea-level and glacial dynamism. Palaeogeogr. Palaeoclimatol. Palaeoecol. 305, 337–351. https://doi.org/10.1016/j.palaeo. 2011.03.026.

Flower, B.P., Kennett, J.P., 1994. The middle Miocene climatic transition: East Antarctic ice sheet development, deep ocean circulation and global carbon cycling. Palaeogeogr. Palaeoclimatol. Palaeoecol. 108, 537–555. https://doi.org/10.1016/0031-0182(94)90251-8. Cenozoic Climate and Paleogeographic Changes in the Pacific Region.

Frimmel, H.E., 2009. Trace element distribution in neoproterozoic carbonates as palaeoenvironmental indicator. Chem. Geol. 258, 338–353. https://doi.org/10.1016/j.chemgeo.2008.10.033.

Froelich, P.N., Klinkhammer, G.P., Bender, M.L., Luedtke, N.A., Heath, G.R., Cullen, D., Dauphin, P., Hammond, D., Hartman, B., Maynard, V., 1979. Early oxidation of organic matter in pelagic sediments of the eastern equatorial Atlantic: suboxic diagenesis. Geochim. Cosmochim. Acta 43, 1075–1090. https://doi.org/10.1016/0016-7037(79)90095-4.

Gilleaudeau, G.J., Kah, L.C., 2013. Carbon isotope records in a Mesoproterozoic epicratonic sea: carbon cycling in a low-oxygen world. Precambrian Res. 228, 85–101. https://doi.org/10.1016/j.precamres.2013.01.006.

Govin, A., Holzwarth, U., Heslop, D., Ford Keeling, L., Zabel, M., Mulitza, S., Collins, J. A., Chiessi, C.M., 2012. Distribution of major elements in Atlantic surface sediments (36°N–49°S): imprint of terrigenous input and continental weathering. Geochem. Geophys. Geosyst. 13, 1–23. https://doi.org/10.1029/2011GC003785.

Guo, Z.T., Ruddiman, W.F., Hao, Q.Z., Wu, H.B., Qiao, Y.S., Zhu, R.X., Peng, S.Z., Wei, J. J., Yuan, B.Y., Liu, T.S., 2002. Onset of Asian desertification by 22 Myr ago inferred from loess deposits in China. Nature 416, 159–163. https://doi.org/10.1038/416159a.

Halfar, J., Mutti, M., 2005. Global dominance of coralline red-algal facies: a response to Miocene oceanographic events. Geology 33, 481–484. https://doi.org/10.1130/G21462.1.

Halfar, J., Godinez-Orta, L., Mutti, M., Valdez-Holguín, J.E., Borges, J.M., 2004. Nutrient and temperature controls on modern carbonate production: an example from the Gulf of California, Mexico. Geology 32, 213–216. https://doi.org/10.1130/G20298.1.

Hallock, P., Schlager, W., 1986. Nutrient excess and the demise of coral reefs and carbonate platforms. PALAIOS 1, 389–398. https://doi.org/10.2307/3514476.

Han, Z., Hu, X., Hu, Z., Jenkyns, H.C., Su, T., 2022. Geochemical evidence from the Kioto Carbonate Platform (Tibet) reveals enhanced terrigenous input and deoxygenation during the early Toarcian. Glob. Planet. Chang. 215, 103887. https://doi.org/10.1016/j.gloplacha.2022.103887.

He, L., Liu, Z., Lyu, X., Ma, P., 2022. Clay mineral assemblages of the oceanic red beds in the northern South China Sea and their responses to the Middle Miocene Climate Transition. Sci. China Earth Sci. 65, 899–909. https://doi.org/10.1007/s11430-021-9878-0.

Higgins, J.A., Blättler, C.L., Lundstrom, E.A., Santiago-Ramos, D.P., Akhtar, A.A., Crüger Ahm, A.-S., Bialik, O., Holmden, C., Bradbury, H., Murray, S.T., Swart, P.K., 2018. Mineralogy, early marine diagenesis, and the chemistry of shallow-water carbonate sediments. Geochim. Cosmochim. Acta 220, 512–534. https://doi.org/10.1016/j.gca.2017.09.046.

Holbourn, A., Kuhnt, W., Clemens, S.C., Heslop, D., 2021. A ~12 Myr Miocene Record of East Asian Monsoon Variability from the South China Sea. Paleoceanogr. Paleoclimatol. 36, e2021PA004267. https://doi.org/10.1029/2021PA004267.

Hood, A.v.S., Planavsky, N.J., Wallace, M.W., Wang, X., 2018. The effects of diagenesis on geochemical paleoredox proxies in sedimentary carbonates. Geochim. Cosmochim. Acta 232, 265–287. https://doi.org/10.1016/j.gca. 2018.04.022.

Hoogakker, B.A.A., Davis, C., Wang, Y., Kusch, S., Nilsson-Kerr, K., Hardisty, D.S., Jacobel, A., Reyes Macaya, D., Glock, N., Ni, S., Sepúlveda, J., Ren, A., Auderset, A., Hess, A.V., Meissner, K.J., Cardich, J., Anderson, R., Barras, C., Basak, C., Bradbury, H.J., Brinkmann, I., Castillo, A., Cook, M., Costa, K., Choquel, C., Diz, P., Donnenfield, J., Elling, F.J., Erdem, Z., Filipsson, H.L., Garrido, S., Gottschalk, J., Govindankutty Menon, A., Groeneveld, J., Hallmann, C., Hendy, I., Hennekam, R., Lu, W., Lynch-Stieglitz, J., Matos, L., Martínez-García, A., Molina, G., Muñoz, P., Moretti, S., Morford, J., Nuber, S., Radionovskaya, S., Raven, M.R., Somes, C.J., Studer, A.S., Tachikawa, K., Tapia, R., Tetard, M., Vollmer, T., Wang, X., Wu, S., Zhang, Y., Zheng, X.-Y., Zhou, Y., 2025. Reviews and syntheses: review of proxies for low-oxygen paleoceanographic reconstructions. Biogeosciences 22, 863–957. https://doi.org/10.5194/bg-22-863-2025.

Huckriede, H., Meischner, D., 1996. Origin and environment of manganese-rich sediments within black-shale basins. Geochim. Cosmochim. Acta 60, 1399–1413. https://doi.org/10.1016/0016-7037(96)00008-7.

Jacobsen, S.B., Kaufman, A.J., 1999. The Sr, C and O isotopic evolution of Neoproterozoic seawater. Chem. Geol. 161, 37–57. https://doi.org/10.1016/S0009-2541(99)00080-7.

Jenkyns, H.C., Géczy, B., Marshall, J.D., 1991. Jurassic manganese carbonates of Central Europe and the Early Toarcian Anoxic Event. J. Geol. 99, 137–149. https://doi.org/10.1086/629481.

Jia, G., Peng, P., Zhao, Q., Jian, Z., 2003. Changes in terrestrial ecosystem since 30 Ma in East Asia: stable isotope evidence from black carbon in the South China Sea. Geology 31, 1093–1096. https://doi.org/10.1130/G19992.1.

Jia, Y., Wu, H., Yan, W., Zhang, C., Hu, B., Zhang, J., Tian, L., Deng, C., 2024. Rare earth element geochemistry of reef carbonates in the South China Sea since the Miocene: insights into paleoclimatic significance. J. Asian Earth Sci. 265, 106094. https://doi.org/10.1016/j.jseaes.2024.106094.

Jiang, H., Wan, S., Ma, X., Zhong, N., Zhao, D., 2017. End-member modeling of the grain-size record of Sikouzi fine sediments in Ningxia (China) and implications for temperature control of Neogene evolution of East Asian winter monsoon. PLoS One 12, e0186153. https://doi.org/10.1371/journal.pone.0186153.

Jiang, W., Yu, K., Fan, T., Xu, S., Wang, R., Zhang, Y., Yue, Y., Zhao, J., Feng, Y., Wei, C., Wang, S., Wang, Y., 2019. Coral reef carbonate record of the Pliocene-Pleistocene climate transition from an atoll in the South China Sea. Mar. Geol. 411, 88–97. https://doi.org/10.1016/j.margeo.2019.02.006.

Jiang, W., Xiao, Y., Yu, K., Wang, R., Xu, S., Guo, N., Gu, T., 2025. Holocene coral reef carbonate REY geochemistry during the neomorphism from aragonite to calcite: a case study in the South China Sea. Palaeogeogr. Palaeoclimatol. Palaeoecol. 665, 112835. https://doi.org/10.1016/j.palaeo.2025.112835.

Keeling, R.F., Körtzinger, A., Gruber, N., 2010. Ocean deoxygenation in a Warming World. Annu. Rev. Mar. Sci. 2, 199–229. https://doi.org/10.1146/annurev.marine.010908.163855.

Kendall, C.G.St.C., Schlager, W., 1981. Carbonates and relative changes in sea level. Mar. Geol. 44, 181–212. https://doi.org/10.1016/0025-3227(81)90118-3. Carbonate Platforms of the Passive-type Continental Margins: Present and Past.

Kender, S., Bogus, K.A., Cobb, T.D., Thomas, D.J., 2018. Neodymium evidence for increased circumpolar deep water flow to the North Pacific during the Middle Miocene Climate Transition. Paleoceanogr. Paleoclimatol. 33, 672–682. https://doi.org/10.1029/2017PA003309.

Kidder, D.L., Erwin, D.H., 2001. Secular distribution of biogenic silica through the phanerozoic: comparison of silica-replaced fossils and bedded cherts at the series level. J. Geol. 109, 509–522. https://doi.org/10.1086/320794.

Land, L.S., 1980. The isotopic and trace element geochemistry of dolomite: the state of the art. In: Zenger, D.H., Dunham, J.B., Ethington, R.L. (Eds.), Concepts and Models of Dolomitization. SEPM Society for Sedimentary Geology, pp. 87–110. https://doi.org/10.2110/pec.80.28.0087.

Lawrence, C.R., Neff, J.C., 2009. The contemporary physical and chemical flux of Aeolian dust: a synthesis of direct measurements of dust deposition. Chem. Geol. 267, 46–63. https://doi.org/10.1016/j.chemgeo.2009.02.005. Combined Ecological and Geologic Perspectives in Ecosystem Studies.

Levin, L.A., 2018. Manifestation, drivers, and emergence of open ocean deoxygenation. Annu. Rev. Mar. Sci. 10, 229–260. https://doi.org/10.1146/annurev-marine-121916-063359.

Lewis, A.R., Marchant, D.R., Ashworth, A.C., Hemming, S.R., Machlus, M.L., 2007. Major middle Miocene global climate change: evidence from East Antarctica and the Transantarctic Mountains. GSA Bull. 119, 1449–1461. https://doi.org/10.1130/0016-7606(2007)119%5B1449:MMMGCC%5D2.0.CO;2.

Li, D., Ling, H.-F., Shields-Zhou, G.A., Chen, X., Cremonese, L., Och, L., Thirlwall, M., Manning, C.J., 2013. Carbon and strontium isotope evolution of seawater across the Ediacaran–Cambrian transition: evidence from the Xiaotan section, NE Yunnan, South China. Precambrian Res. 225, 128–147. https://doi.org/10.1016/j.precamres.2012.01.002. Biogeochemical changes across the Ediacaran-Cambrian transition in South China.

Li, Q., Wu, S., Xia, D., You, X., Zhang, H., Lu, H., 2020. Major and trace element geochemistry of the lacustrine organic-rich shales from the Upper Triassic Chang 7 Member in the southwestern Ordos Basin, China: implications for paleoenvironment and organic matter accumulation. Mar. Pet. Geol. 111, 852–867. https://doi.org/10.1016/j.marpetgeo.2019.09.003.

Li, S., Nie, J., Ren, X., Xing, L., Tong, F., Xiao, Y., 2023a. Increased primary mineral dissolution control on a terrestrial silicate lithium isotope record during the middle Miocene climate optimum. Geochim. Cosmochim. Acta 348, 41–53. https://doi.org/10.1016/j.gca.2023.03.009.

Li, M., Wan, S., Colin, C., Jin, H., Zhao, D., Pei, W., Jiao, W., Tang, Y., Tan, Y., Shi, X., Li, A., 2023b. Expansion of C4 plants in South China and evolution of East Asian monsoon since 35 Ma: black carbon records in the northern South China Sea. Glob. Planet. Chang. 223, 104079. https://doi.org/10.1016/j.gloplacha. 2023.104079.

Liu, Y., Sun, L., Zhou, X., Luo, Y., Huang, W., Yang, C., Wang, Y., Huang, T., 2014. A 1400-year terrigenous dust record on a coral island in South China Sea. Sci. Rep. 4, 4994. https://doi.org/10.1038/srep04994.

Liu, Y., Wu, S., Li, X., Chen, W., Han, X., Yang, C., Qin, Y., Huang, X., Yang, Z., Sun, J., Zhu, L., 2023. Seismic stratigraphy and development of a modern isolated carbonate platform (Xuande Atoll) in the South China Sea. Front. Earth Sci. 10, 1042371. https://doi.org/10.3389/feart.2022.1042371.

Liu, F., Du, J., Huang, E., Ma, W., Ma, X., Lourens, L.J., Tian, J., 2024. Accelerated marine carbon cycling forced by tectonic degassing over the Miocene climate optimum. Sci. Bull. 69, 823–832. https://doi.org/10.1016/j.scib.2023.12.052.

Liu, X., Sun, X., Sun, W., Hao, Y., Huang, J., 2025. A link between the paleoenvironment and PETM via trace element proxies in Southwest Atlantic sediments. Glob. Planet. Chang. 248, 104774. https://doi.org/10.1016/j.gloplacha.2025.104774.

Lu, Y., Huang, B., Chen, F., 2026. Variations in thermocline depth and their response to the East Asian Monsoon in the Northern South China Sea during the Early-Middle Miocene: evidence from planktonic foraminifera. Mar. Geol. 493, 107721. https://doi.org/10.1016/j.margeo.2026.107721.

Ma, L., Sun, Y., Jin, Z., Bao, Z., Yuan, H., Zhang, P., Huang, K.-J., 2022. Magnesium isotopic evidence for staged enhancement of the East Asian Summer Monsoon precipitation since the Miocene. Geochim. Cosmochim. Acta 324, 140–155. https://doi.org/10.1016/j.gca.2022.03.005.

Ma, P., Ma, C., Yang, S., Fernandez, A.R., 2023. East Asian summer monsoon evolution recorded by the middle Miocene pelagic reddish clay, South China Sea. Glob. Planet. Chang. 222, 104072. https://doi.org/10.1016/j.gloplacha.2023.104072.

McConnaughey, T., 1989. 13C and 18O isotopic disequilibrium in biological carbonates: I. Patterns. Geochim. Cosmochim. Acta 53, 151–162. https://doi.org/10.1016/0016-7037(89)90282-2.

Meng, M., Yu, K., Hallock, P., Qin, G., Jiang, W., Fan, T., 2022. Foraminifera indicate Neogene evolution of Yongle Atoll from Xisha Islands in the South China Sea. Palaeogeogr. Palaeoclimatol. Palaeoecol. 602, 111163. https://doi.org/10.1016/j.palaeo.2022.111163.

Miao, Y., Fang, X., Herrmann, M., Wu, F., Zhang, Y., Liu, D., 2011. Miocene pollen record of KC-1 core in the Qaidam Basin, NE Tibetan Plateau and implications for evolution of the East Asian monsoon. Palaeogeogr. Palaeoclimatol. Palaeoecol. 299, 30–38. https://doi.org/10.1016/j.palaeo.2010.10.026.

Miller, K.G., Browning, J.V., Schmelz, W.J., Kopp, R.E., Mountain, G.S., Wright, J.D., 2020. Cenozoic sea-level and cryospheric evolution from deep-sea geochemical and continental margin records. Sci. Adv. 6, eaaz1346. https://doi.org/10.1126/sciadv.aaz1346.

Nothdurft, L.D., Webb, G.E., Kamber, B.S., 2004. Rare earth element geochemistry of Late Devonian reefal carbonates, Canning Basin, Western Australia: confirmation of a seawater REE proxy in ancient limestones. Geochim. Cosmochim. Acta 68, 263–283. https://doi.org/10.1016/S0016-7037(03)00422-8.

Okafor, M.-M., Azmy, K., 2024. Redox conditions across the Upper Cambrian of eastern Laurentia: implications from geochemical proxies. Palaeogeogr. Palaeoclimatol. Palaeoecol. 637, 111978. https://doi.org/10.1016/j.palaeo. 2023.111978.

Ortega-Ariza, D., Franseen, E.K., Boudagher-Fadel, M.K., 2021. Effects of sea level and upwelling on development of a Miocene shallow-water tropical carbonate ramp system, Ponce, Puerto Rico. J. Sediment. Res. 91, 1227–1256. https://doi.org/10.2110/jsr.2020.200.

Pogge von Strandmann, P.A.E., Jenkyns, H.C., Woodfine, R.G., 2013. Lithium isotope evidence for enhanced weathering during Oceanic Anoxic Event 2. Nat. Geosci. 6, 668–672. https://doi.org/10.1038/ngeo1875.

Prell, W.L., Kutzbach, J.E., 1992. Sensitivity of the Indian monsoon to forcing parameters and implications for its evolution. Nature 360, 647–652. https://doi.org/10.1038/360647a0.

Qin, Y., Wu, S., Betzler, C., 2022. Backstepping patterns of an isolated carbonate platform in the northern South China Sea and its implication for paleoceanography and paleoclimate. Mar. Pet. Geol. 146, 105927. https://doi.org/10.1016/j.marpetgeo.2022.105927.

Rea, D.K., 1994. The paleoclimatic record provided by Eolian deposition in the deep sea: the geologic history of wind. Rev. Geophys. 32, 159–195. https://doi.org/10.1029/93RG03257.
Rimmer, S.M., 2004. Geochemical paleoredox indicators in Devonian–Mississippian black shales, Central Appalachian Basin (USA). Chem. Geol. 206, 373–391. https://doi.org/10.1016/j.chemgeo.2003.12.029. Geochemistry of Organic-Rich Shales: New Perspectives.
Shao, L., Cui, Y., Qiao, P., Zhang, D., Liu, X., Zhang, C., 2017a. Sea-level changes and carbonate platform evolution of the Xisha Islands (South China Sea) since the Early Miocene. Palaeogeogr. Palaeoclimatol. Palaeoecol. 485, 504–516. https://doi.org/10.1016/j.palaeo.2017.07.006.
Shao, L., Li, Q., Zhu, W., Zhang, D., Qiao, P., Liu, X., You, L., Cui, Y., Dong, X., 2017b. Neogene carbonate platform development in the NW South China Sea: Litho-, bio- and chemo-stratigraphic evidence. Mar. Geol. 385, 233–243. https://doi.org/10.1016/j.margeo.2017.01.009.
Shembilu, N.C., Azmy, K., 2022. Trace element variations across Middle–Upper Cambrian carbonates: implications for the paleoenvironment of eastern Laurentia. Mar. Pet. Geol. 135, 105385. https://doi.org/10.1016/j.marpetgeo.2021.105385.
Shevenell, A.E., Kennett, J.P., Lea, D.W., 2004. Middle Miocene Southern Ocean cooling and antarctic cryosphere expansion. Science 305, 1766–1770. https://doi.org/10.1126/science.1100061.
Shevenell, A.E., Kennett, J.P., Lea, D.W., 2008. Middle Miocene ice sheet dynamics, deep-sea temperatures, and carbon cycling: a Southern Ocean perspective. Geochem. Geophys. Geosyst. 9, 1–14. https://doi.org/10.1029/2007GC001736.
Shu, W., Liu, Z., Colin, C., Ma, P., Huang, B., Dapoigny, A., 2023. Terrigenous provenance of late Oligocene–Miocene sediments in the central basin of the South China Sea and its implications for chemical weathering and climate change. Mar. Geol. 462, 107098. https://doi.org/10.1016/j.margeo.2023.107098.
Smrzka, D., Zwicker, J., Bach, W., Feng, D., Himmler, T., Chen, D., Peckmann, J., 2019. The behavior of trace elements in seawater, sedimentary pore water, and their incorporation into carbonate minerals: a review. Facies 65, 41. https://doi.org/10.1007/s10347-019-0581-4.
Song, Haijun, Wignall, P.B., Song, Huyue, Dai, X., Chu, D., 2019. Seawater temperature and dissolved oxygen over the past 500 million years. J. Earth Sci. 30, 236–243. https://doi.org/10.1007/s12583-018-1002-2.
Steinmann, J.W., Grammer, G.M., Brunner, B., Jones, C.K., Riedinger, N., 2020. Assessing the application of trace metals as paleoproxies and a chemostratigraphic tool in carbonate systems: a case study from the “Mississippian Limestone” of the midcontinent, United States. Mar. Pet. Geol. 112, 104061. https://doi.org/10.1016/j.marpetgeo.2019.104061.
Steinthorsdottir, M., Coxall, H.K., de Boer, A.M., Huber, M., Barbolini, N., Bradshaw, C. D., Burls, N.J., Feakins, S.J., Gasson, E., Henderiks, J., Holbourn, A.E., Kiel, S., Kohn, M.J., Knorr, G., Kürschner, W.M., Lear, C.H., Liebrand, D., Lunt, D.J., Mörs, T., Pearson, P.N., Pound, M.J., Stoll, H., Strömberg, C.A.E., 2021. The Miocene: the future of the past. Paleoceanogr. Paleoclimatol. 36, e2020PA004037. https://doi.org/10.1029/2020PA004037.
Su, T., Farnsworth, A., Spicer, R.A., Huang, J., Wu, F.-X., Liu, J., Li, S.-F., Xing, Y.-W., Huang, Y.-J., Deng, W.-Y.-D., Tang, H., Xu, C.-L., Zhao, F., Srivastava, G., Valdes, P. J., Deng, T., Zhou, Z.-K., 2019. No high Tibetan Plateau until the Neogene. Sci. Adv. 5, eaav2189. https://doi.org/10.1126/sciadv.aav2189.
Su, X., Xiang, R., Yi, L., Zhang, Y., Qin, G., Yan, W., 2024. Neogene carbonate platform development in the southern South China Sea: evidence from calcareous microfossils. Palaeogeogr. Palaeoclimatol. Palaeoecol. 640, 112093. https://doi.org/10.1016/j.palaeo.2024.112093.
Swart, P.K., 1983. Carbon and oxygen isotope fractionation in scleractinian corals: a review. Earth Sci. Rev. 19, 51–80. https://doi.org/10.1016/0012-8252(83)90076-4.
Swart, P.K., 2015. The geochemistry of carbonate diagenesis: the past, present and future. Sedimentology 62, 1233–1304. https://doi.org/10.1111/sed.12205.
Swart, P.K., Blättler, C.L., Nakakuni, M., Mackenzie, G.J., Betzler, C., Eberli, G.P., Reolid, J., Alonso-García, M., Slagle, A.L., Wright, J.D., Kroon, D., Reijmer, J.J.G., Hui Mee, A.L., Young, J.R., Alvarez-Zarikian, C.A., Bialik, O.M., Guo, J.A., Haffen, S., Horozal, S., Inoue, M., Jovane, L., Lanci, L., Laya, J.C., Lüdmann, T., Nagender Nath, B., Niino, K., Petruny, L.M., Pratiwi, S.D., Su, X., Sloss, C.R., Yao, Z., 2019. Cyclic anoxia and organic rich carbonate sediments within a drowned carbonate platform linked to Antarctic ice volume changes: Late Oligocene-early Miocene Maldives. Earth Planet. Sci. Lett. 521, 1–13. https://doi.org/10.1016/j.epsl.2019.05.019.
Taylor, S.R., McLennan, S.M., 1985. The Continental Crust: Its Composition and Evolution, an Examination of the Geochemical Record Preserved in Sedimentary Rocks. Blackwell Scientific Pub, United States, p. 311.
Torfstein, A., Steinberg, J., 2020. The Oligo–Miocene closure of the Tethys Ocean and evolution of the proto-Mediterranean Sea. Sci. Rep. 10, 13817. https://doi.org/10.1038/s41598-020-70652-4.
Tribovillard, N., Algeo, T.J., Lyons, T., Riboulleau, A., 2006. Trace metals as paleoredox and paleoproductivity proxies: an update. Chem. Geol. 232, 12–32. https://doi.org/10.1016/j.chemgeo.2006.02.012.
van de Wal, R.S.W., de Boer, B., Lourens, L.J., Köhler, P., Bintanja, R., 2011. Reconstruction of a continuous high-resolution CO_2 record over the past 20 million years. Clim. Past 7, 1459–1469. https://doi.org/10.5194/cp-7-1459-2011.
Veizer, J., Ala, D., Azmy, K., Bruckschen, P., Buhl, D., Bruhn, F., Carden, G.A.F., Diener, A., Ebneth, S., Godderis, Y., Jasper, T., Korte, C., Pawellek, F., Podlaha, O.G., Strauss, H., 1999. 87Sr/86Sr, δ13C and δ18O evolution of Phanerozoic seawater. Chem. Geol. 161, 59–88. https://doi.org/10.1016/S0009-2541(99)00081-9.
Viehmann, S., Kujawa, R., Hohl, S.V., Tepe, N., Rodler, A.S., Hofmann, T., Draganits, E., 2023. Stromatolitic carbonates from the Middle Miocene of the western Pannonian Basin reflect trace metal availability in microbial habitats during the Badenian Salinity Crisis. Chem. Geol. 618, 121301. https://doi.org/10.1016/j.chemgeo.2023.121301.
Wan, S., Li, A., Clift, P.D., Stuut, J.-B.W., 2007. Development of the East Asian monsoon: mineralogical and sedimentologic records in the northern South China Sea since 20 Ma. Palaeogeogr. Palaeoclimatol. Palaeoecol. 254, 561–582. https://doi.org/10.1016/j.palaeo.2007.07.009.
Wan, S., Kürschner, W.M., Clift, P.D., Li, A., Li, T., 2009. Extreme weathering/erosion during the Miocene Climatic Optimum: evidence from sediment record in the South China Sea. Geophys. Res. Lett. 36, L19706. https://doi.org/10.1029/2009GL040279.
Wan, S., Zhao, D., Jin, H., Sha, Y., Shi, Z., Clift, P.D., Jian, Z., Liu, C., Zarikian, C.A., France-Lanord, C., Yu, Z., Zhang, J., Jiao, W., Yin, X., Li, A., 2025. Interactive forces of temperature and topographic uplift shaped the East Asian monsoon rainfall evolution since the Oligocene. Innov. Geosci. 3, 100141-9. https://doi.org/10.59717/j.xinn-geo.2025.100141.
Wang, B., Clemens, S.C., Liu, P., 2003. Contrasting the Indian and East Asian monsoons: implications on geologic timescales. Mar. Geol. 201, 5–21. https://doi.org/10.1016/S0025-3227(03)00196-8.
Warny, S., Askin, R.A., Hannah, M.J., Mohr, B.A.R., Raine, J.I., Harwood, D.M., Florindo, F., the SMS Science Team, 2009. Palynomorphs from a sediment core reveal a sudden remarkably warm Antarctica during the middle Miocene. Geology 37, 955–958. https://doi.org/10.1130/G30139A.1.
Webb, G.E., Kamber, B.S., 2000. Rare earth elements in Holocene reefal microbialites: a new shallow seawater proxy. Geochim. Cosmochim. Acta 64, 1557–1565. https://doi.org/10.1016/S0016-7037(99)00400-7.
Weber, J.N., Woodhead, P.M.J., 1969. Factors affecting the carbon and oxygen isotopic composition of marine carbonate sediments—II. Heron Island, Great Barrier Reef, Australia. Geochim. Cosmochim. Acta 33, 19–38. https://doi.org/10.1016/0016-7037(69)90090-8.
Webster, P.J., 1994. The role of hydrological processes in ocean-atmosphere interactions. Rev. Geophys. 32, 427–476. https://doi.org/10.1029/94RG01873.
Wei, G., Li, X.-H., Liu, Y., Shao, L., Liang, X., 2006. Geochemical record of chemical weathering and monsoon climate change since the early Miocene in the South China Sea. Paleoceanography 21, 4214. https://doi.org/10.1029/2006PA001300.
Westerhold, T., Marwan, N., Drury, A.J., Liebrand, D., Agnini, C., Anagnostou, E., Barnet, J.S.K., Bohaty, S.M., De Vleeschouwer, D., Florindo, F., Frederichs, T., Hodell, D.A., Holbourn, A.E., Kroon, D., Lauretano, V., Littler, K., Lourens, L.J., Lyle, M., Pälike, H., Röhl, U., Tian, J., Wilkens, R.H., Wilson, P.A., Zachos, J.C., 2020. An astronomically dated record of Earth’s climate and its predictability over the last 66 million years. Science 369, 1383–1387. https://doi.org/10.1126/science.aba6853.
White, A.F., Blum, A.E., 1995. Effects of climate on chemical weathering in watersheds. Geochim. Cosmochim. Acta 59, 1729–1747. https://doi.org/10.1016/0016-7037(95)00078-E.
Wilson, M.E.J., 2002. Cenozoic carbonates in Southeast Asia: implications for equatorial carbonate development. Sediment. Geol. 147, 295–428. https://doi.org/10.1016/S0037-0738(01)00228-7.
Wilson, M.E.J., 2008. Global and regional influences on equatorial shallow-marine carbonates during the Cenozoic. Palaeogeogr. Palaeoclimatol. Palaeoecol. 265, 262–274. https://doi.org/10.1016/j.palaeo.2008.05.012.
Wittkop, C., Swanner, E.D., Grengs, A., Lambrecht, N., Fakhraee, M., Myrbo, A., Bray, A. W., Poulton, S.W., Katsev, S., 2020. Evaluating a primary carbonate pathway for manganese enrichments in reducing environments. Earth Planet. Sci. Lett. 538, 116201. https://doi.org/10.1016/j.epsl.2020.116201.
Wu, F., Xie, X., Betzler, C., Zhu, W., Zhu, Y., Guo, L., Ma, Z., Bai, H., Ma, B., 2019a. The impact of eustatic sea-level fluctuations, temperature variations and nutrient-level changes since the Pliocene on tropical carbonate platform (Xisha Islands, South China Sea). Palaeogeogr. Palaeoclimatol. Palaeoecol. 514, 373–385. https://doi.org/10.1016/j.palaeo.2018.10.013.
Wu, F., Xie, X., Li, X., Betzler, C., Shang, Z., Cui, Y., 2019b. Carbonate factory turnovers influenced by the monsoon (Xisha Islands, South China Sea). J. Geol. Soc. Lond. 176, 885–897. https://doi.org/10.1144/jgs2018-086.
Wu, F., Xie, X., Zhu, Y., Coletti, G., Betzler, C., Cui, Y., Bai, H., Chen, B., Shang, Z., 2021. Early development of carbonate platform (Xisha Islands) in the northern South China Sea. Mar. Geol. 441, 106629. https://doi.org/10.1016/j.margeo.2021.106629.
Wu, L., Wang, R., Yu, K., Ren, M., Booker, S., Shen, R., Jiang, W., Xu, S., Fan, T., Wu, S., Qin, Q., Li, X., 2024. Meteoric diagenesis influenced by East Asian Summer Monsoon: a case study from the Pleistocene carbonate succession, Xisha Islands, South China Sea. Palaeogeogr. Palaeoclimatol. Palaeoecol. 633, 111882. https://doi.org/10.1016/j.palaeo.2023.111882.
Wu, J., Guo, L., Xiong, S., Yang, S., Yang, X., Zhang, Y., Zhang, M., Zhang, Q., Cui, J., Jiang, W., Zhang, B., 2025. Enhanced continental weathering contributed to the termination of the Middle Miocene Climatic Optimum. Geophys. Res. Lett. 52, e2025GL118302. https://doi.org/10.1029/2025GL118302.
Xie, S.-P., Xie, Q., Wang, D., Liu, W.T., 2003. Summer upwelling in the South China Sea and its role in regional climate variations. J. Geophys. Res. Oceans 108, 1–17. https://doi.org/10.1029/2003JC001867.
Xu, S., Yu, K., Fan, T., Jiang, W., Wang, R., Zhang, Y., Yue, Y., Wang, S., 2019. Coral reef carbonate $\delta^{13}C$ records from the northern South China Sea: a useful proxy for seawater $\delta^{13}C$ and the carbon cycle over the past 1.8 Ma. Glob. Planet. Chang. 182, 103003. https://doi.org/10.1016/j.gloplacha.2019.103003.
Xue, L., Ding, X., Pei, R., Wan, X., 2019. Miocene paleoenvironmental evolution based on benthic foraminiferal assemblages in the Lufeng Sag, northern South China Sea. Acta Oceanol. Sin. 38, 124–137. https://doi.org/10.1007/s13131-019-1405-7.
Yang, Y., Yu, K., Wang, R., Fan, T., Jiang, W., Xu, S., Li, Y., Zhao, J., 2022. 87Sr/86Sr of coral reef carbonate strata as an indicator of global sea level fall: evidence from a

928.75-m-long core in the South China Sea. Mar. Geol. 445, 106758. https://doi.org/10.1016/j.margeo.2022.106758.

Yang, Y., Yu, K., Xiong, B., Jiang, W., Xu, S., Wang, R., Fan, T., 2025. Characteristics and primary controls of coral reef carbonate karstification in the South China Sea since the Miocene. Front. Mar. Sci. 12, 1619169. https://doi.org/10.3389/fmars.2025.1619169.

Yu, K., 2012. Coral reefs in the South China Sea: their response to and records on past environmental changes. Sci. China Earth Sci. 55, 1217–1229. https://doi.org/10.1007/s11430-012-4449-5.

Zachos, J., Pagani, M., Sloan, L., Thomas, E., Billups, K., 2001. Trends, rythms and abberations in global climate 65 Ma to present. Science 292, 686–693. https://doi.org/10.1126/science.1059412.

Zhang, K., Shields, G.A., Zhou, Y., Strauss, H., Struck, U., Jensen, S., 2024. The basal Cambrian carbon isotope excursion revealed in the Central Iberian Zone, Spain. Precambrian Res. 411, 107526. https://doi.org/10.1016/j.precamres.2024.107526.

Zhang, Z., Liu, S., Zhao, Y., Zhang, Y., Liu, C., Wei, H., Zhang, G., Yang, J., Guo, X., Li, S., 2025. Enhanced Deep-Water Oxygenation in the South China Sea driven by Middle Miocene climate cooling. Paleoceanogr. Paleoclimatol. 40, e2025PA005120. https://doi.org/10.1029/2025PA005120.

Zhao, M.-Y., Zheng, Y.-F., 2014. Marine carbonate records of terrigenous input into Paleotethyan seawater: geochemical constraints from Carboniferous limestones. Geochim. Cosmochim. Acta 141, 508–531. https://doi.org/10.1016/j.gca.2014.07.001.

Zhao, Q., Wang, P., Cheng, X., Wang, J., Huang, B., Xu, J., Zhou, Z., Jian, Z., 2001. A record of Miocene carbon excursions in the South China Sea. Sci. China Ser. D Earth Sci. 44, 943–951. https://doi.org/10.1007/BF02907087.

Zhao, H., Sun, Y., Qiang, X., 2017. Iron oxide characteristics of mid-Miocene Red Clay deposits on the western Chinese Loess Plateau and their paleoclimatic implications. Palaeogeogr. Palaeoclimatol. Palaeoecol. 468, 162–172. https://doi.org/10.1016/j.palaeo.2016.12.008.

Zhao, Y., Luo, Y., Zhang, Y., Li, G., Webster, J.M., Xu, W., Yan, W., 2026. Carbonate platform evolution of the Meiji Atoll in the Southern South China Sea since the late Miocene. Minerals 16, 205. https://doi.org/10.3390/min16020205.

Zhou, C., Zhao, W., Tian, J., Zhao, X., Zhu, Y., Yang, Q., Qu, T., 2017. Deep western boundary current in the South China Sea. Sci. Rep. 7, 9303. https://doi.org/10.1038/s41598-017-09436-2.

Zhou, K., Sun, J., Yang, M., Zhang, S., Wang, Weichao, Gao, R., Zhang, P., Wang, Wanqing, Liu, H., Shao, L., Lu, J., 2023a. Geochemical characteristics of the Middle Jurassic Coal-Bearing mudstones in the Dameigou Area (Qaidam Basin, NW China): implications for paleoclimate, paleoenvironment, and organic matter accumulation. ACS Omega 8, 47540–47559. https://doi.org/10.1021/acsomega.3c05433.

Zhou, C., Xiao, X., Zhao, W., Yang, J., Huang, X., Guan, S., Zhang, Z., Tian, J., 2023b. Increasing deep-water overflow from the Pacific into the South China Sea revealed by mooring observations. Nat. Commun. 14, 2013. https://doi.org/10.1038/s41467-023-37767-4.

Zhu, X., Li, G., Tian, Y., Xu, W., Miao, L., Liu, J., Luo, Y., Cheng, J., Zhang, L., Wang, S., Yan, W., 2022. Production of short-chain *n*-fatty acids in coral reefs in the southern South China Sea since the Late Miocene. Palaeogeogr. Palaeoclimatol. Palaeoecol. 592, 110898. https://doi.org/10.1016/j.palaeo.2022.110898.